NPOESS Aircraft Sounder Testbed-Microwave (NAST-M): Instrument Description and Initial Flight Results

William J. Blackwell, *Student Member, IEEE*, John W. Barrett, Frederick W. Chen, *Student Member, IEEE*, R. Vincent Leslie, *Student Member, IEEE*, Philip W. Rosenkranz, *Fellow, IEEE*, Michael J. Schwartz, and David H. Staelin, *Fellow, IEEE*

***Abstract*—The National Polar-Orbiting Operational Environmental Satellite System (NPOESS) aircraft sounder testbed (NAST) has recently been developed and deployed on the NASA ER-2 high-altitude aircraft. The testbed consists of two co-located cross-track scanning instruments: a Fourier transform interferometer spectrometer (NAST-I) [1] with spectral coverage of 3.7–15.5 μm and a passive microwave spectrometer (NAST-M) with 17 channels near the oxygen absorption lines at 50–57 GHz and 118.75 GHz. The testbed provides the first coregistered imagery from high-resolution microwave and infrared sounders and will provide new data that will help 1) validate meteorological satellite environmental data record (EDR) feasibility, 2) define future satellite instrument specifications, and 3) demonstrate operational issues in ground validation, data calibration, and retrievals of meteorological parameters. To help validate the performance and potential of NAST-M, imagery was collected from more than 20 overpasses of hurricanes Bonnie and Earl during the Convection and Moisture Experiment (CAMEX-3), Florida, Summer 1998. The warm core and convection morphology of Hurricane Bonnie (August, 1998) is clearly revealed both by aircraft-based microwave brightness temperature imagery and temperature retrievals within the eye. Radiance comparisons with the Advanced Microwave Sounding Unit (AMSU) on the NOAA-15 satellite and radiosonde observations yield root mean-squared (RMS) agreements of approximately 1 K or less.**

***Index Terms*—Aircraft instrumentation, hurricane images, microwave imaging, microwave radiometry, precipitation, temperature profile retrievals.**

I. Introduction

AIRCRAFT-BASED imaging of temperature and precipitation using passive microwave radiometry has been studied by a number of investigators (see [2]–[4] for example). Multispectral microwave sounders exploit the frequency dependence of scattering from hydrometeors to provide information about particle sizes [5], cloud-top altitudes [3], and rain rates [6]. Recent studies [4] have demonstrated the ability of high-resolution microwave imagery to clearly resolve hurricane eyewalls and warm cores within the eyes. In this paper, the NAST-M instrument is described and representative imagery collected over Hurricane Bonnie on August 23 and August 26, 1998 is examined. Data from NAST-M are also compared with data from a coincident NOAA-15 AMSU overpass which occurred on March 26, 1999 (00:41:30 UTC, 47.1309° N, −86.9670° W) during Winter Experiment (WINTEX), Wisconsin, March–April 1999.

Manuscript received September 29, 2000; revised September 5, 2001. This work was supported in part by a National Science Foundation Graduate Research Fellowship, NASA Grant NAG5-7487, NASA/GSFC Contract NAS5-31376, the Lincoln Laboratory, Massachusetts Institute of Technology, Lexington, under PO BX-7601 and AF Prime Contract F19628-00-C-0002. Opinions, interpretations, conclusions, and recommendations are those of the authors and are not necessarily endorsed by the United States government.

W. J. Blackwell, J. W. Barrett, F. W. Chen, R. V. Leslie, P. W. Rosenkranz, and D. H. Staelin are with the Research Laboratory of Electronics, Massachusetts Institute of Technology, Cambridge, MA 02139 USA (e-mail: staelin@ll.mit.edu).

M. J. Schwartz is with Jet Propulsion Laboratory, California Institute of Technology, Pasadena, CA 91109-8099 USA.

Publisher Item Identifier S 0196-2892(01)10411-0.

II. Instrument Overview

The NAST-M instrument consists of two independent total-power radiometer systems that share a cross-track scanning reflector. The first radiometer (henceforth referred to as the "54-GHz radiometer") is a single-sideband system with eight channels from 50.3 GHz to 56.02 GHz, and the second radiometer (henceforth referred to as the "118-GHz radiometer") is a double-sideband system with nine channels from 118.75 ± 0.120 GHz to 118.75 ± 3.5 GHz. Both radiometers measure a single linear polarization. The electric field is oriented along-track at nadir and rotates with the scan angle. The package typically flies unpressurized at a nominal ER-2 cruising altitude of approximately 20 km at a speed of ∼200 m/s. The NAST configuration, as flown in the NASA ER-2, is shown in Fig. 1. The NAST-M instrument, complete with all supporting flight hardware, weighs approximately 225 lbs., occupies a volume of approximately 15 ft^3, and consumes approximately 1.5 kW @ 120 VAC (1.2 kW of which is for heaters).

A. Radiometer Systems

A block diagram of the 54-GHz radiometer system is shown in Fig. 2. The 118-GHz system is conceptually identical, except for the absence of the low-noise RF amplifier. Both systems utilize superheterodyne receivers. The local oscillator (LO) frequencies are 46 GHz and 118.75 GHz. Both LOs are temperature-controlled using thermo-electric devices to prevent frequency drift, and all amplifiers are temperature-controlled to prevent gain drift. The gain as a function of input power of the IF amplifiers, video amplifiers, square-law detectors, and A/D converters was measured [7] and found to be linear to within instrument thermal noise. The calibration and noise performance of the three channels closest to the 118.75-GHz line is degraded by LO power which is reflected off the calibration targets and

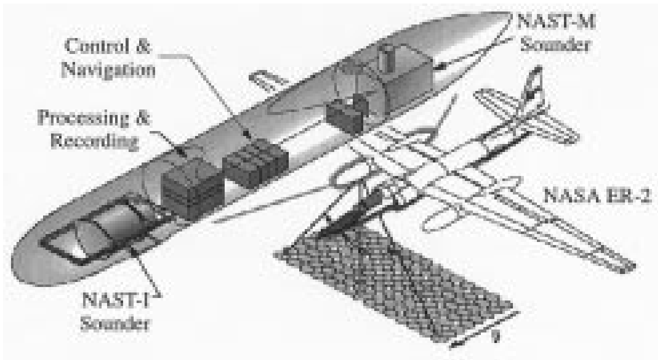

Fig. 1. NAST ER-2 configuration.

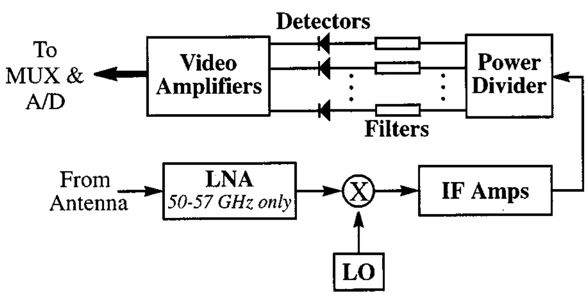

Fig. 2. Radiometer block diagram.

TABLE I
CHANNEL SPECIFICATIONS FOR THE 54-GHz RADIOMETER

No.	Frequency (GHz)	Bandwidth (MHz)	Sensitivity (RMS K)	Offset from AMSU (K)
1	50.30	180	0.21	0.1
2	51.76	400	0.13	0.3
3	52.80	400	0.12	0.4
4	53.75	240	0.16	0.5
5	54.40	400	0.13	-0.5
6	54.94	400	0.15	-0.4
7	55.50	330	0.18	-0.2
8	56.02	270	0.18	-0.1

re-enters the antenna feed, stimulating instabilities involving the preamplifiers. These instabilities are partially remedied by means of a small capacitor placed in series with the preamplifier input. Additional similar radiometer systems operating near the 183-GHz water vapor line and the 425-GHz oxygen line are presently being added to the NAST-M package. Channel specifications for the 54-GHz and 118-GHz radiometers are given in Tables I and II. Values for channel sensitivities include errors due to noisy calibration measurements. Brightness temperature offsets based on a March 26, 1999 AMSU overpass are also shown (see Section III-A). Temperature weighting functions for the channels of both radiometers are shown in Fig. 3.

B. Field of View

The NAST-M scanning subassembly is shown in Fig. 4. The 3-dB (full-width at half-max) beamwidth for both antenna beams is 7.5° (2.6-km nadir footprint diameter at an altitude of 20 km). The downward-looking port of NAST-M allows an unobstructed view for nadir ±65°, which yields a cross-track swath width of approximately 100 km from an altitude of 20 km. The reflector is stepped through a full rotation approximately every 5.5 s. A single scan consists of 19 spots across nadir ±65° and three calibration spots: a heated internal blackbody, an ambient internal blackbody, and a zenith view through a port in the top of the instrument of the cosmic background. The nominal integration time for all spots (including calibration spots) is 100 ms.

TABLE II
CHANNEL SPECIFICATIONS FOR THE 118-GHz RADIOMETER

No.	Frequency Offset (MHz)	Bandwidth (MHz)	Sensitivity (RMS K)	Offset from AMSU (K)
1	± 3500	1000	0.19	0.7
2	± 2550	500	0.23	0.9
3	± 2050	500	0.21	0.7
4	± 1600	400	0.25	0.6
5	± 1200	400	0.28	0.7
6	± 800	400	0.34	0.9
7	± 450	300	0.45	> 2
8	± 235	130	0.90	> 5
9	± 120	100	1.17	> 10

C. Internal Calibration Targets

Two blackbody calibration targets (20 cm × 20 cm × 4 cm) were fabricated from aluminum and iron-loaded epoxy. Both loads have surfaces covered with tessellated pyramids machined from Emerson–Cuming CR-112 Eccosorb that are 12-mm tall with square bases with 8-mm sides. The aluminum backing extends up into the cores of the pyramids to minimize temperature gradients between pyramid bases and tips. Rectangular channels with square edges 4-mm wide and 3-mm deep were cut into the aluminum, thereby increasing the volume of absorbing material at the base of the pyramids and increasing return loss with negligible change in thermal conductivity. Thin-film platinum resistive temperature device (RTD) sensors were placed on the surface of the Eccosorb, embedded in the Eccosorb, and epoxied to the back of the aluminum. The temperature sensors were calibrated to an accuracy of ±0.05 K. The loads are insulated on the front with a 1-cm thick layer of Styrofoam and on the back and sides with extruded polystyrene. Time-domain reflectometry measurements at 75–110 GHz yield average return losses exceeding 30 dB (emissivity of 0.999). The thermodynamic temperature of the heated target is maintained at an average temperature of 334 ± 0.1 K and the thermodynamic temperature of the ambient target is typically 245 ± 5 K at altitude. While the thermodynamic temperature of the cosmic background is 2.736 ± 0.02 K, the measured brightness temperature can range from 2.9 ± 0.05 K for the most-transparent channel to 150 ± 5 K for the least transparent channel, depending on aircraft altitude.

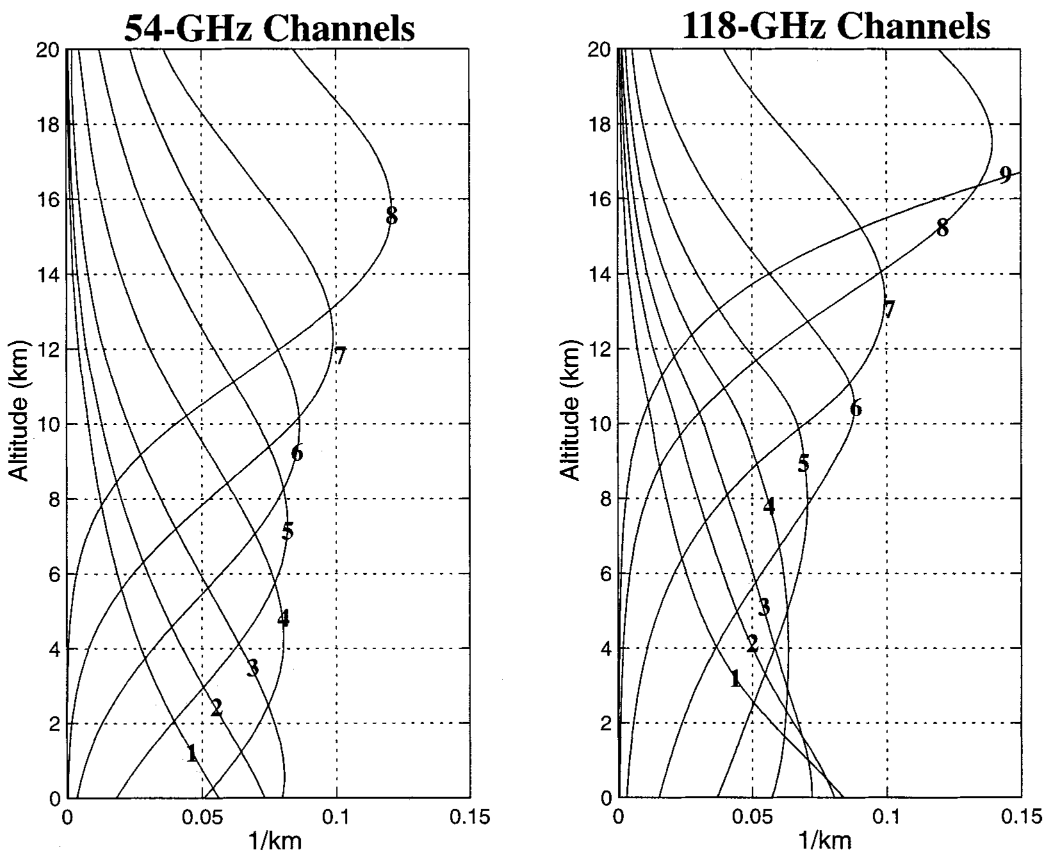

Fig. 3. NAST-M clear-air temperature weighting functions (downward-looking). The U.S. 1976 Standard Atmosphere over a black surface was assumed for the calculations.

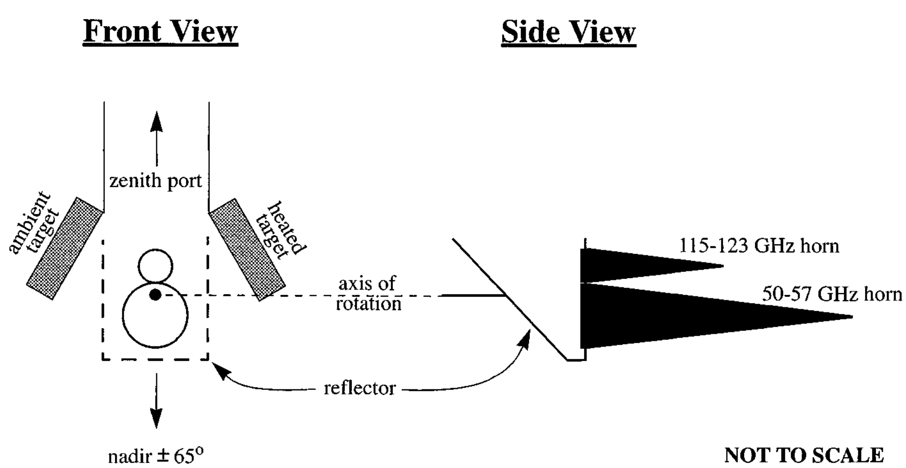

Fig. 4. NAST-M scanning subassembly.

D. Control and Data Handling

Instrument control and data collection tasks are coordinated by a microcomputer with an AMD 5 × 86 processor incorporating a flash-RAM hard drive and PC104 A/D cards. The Real-Time Linux [8] operating system was used. Built-in TCP/IP support allows real-time instrument control (via satellite uplink on the ER-2) and postflight data download via Ethernet.

E. Digital Video System

A wide-angle (111°), high-resolution (640 × 480 pixels/frame) video camera (Panasonic GP-KS162 with GP-LM3TA lens) is flown with the microwave package to provide continuous imagery of clouds and surface conditions. The video output is digitized (24-bit RGB) by a frame grabber board (one frame every 5 s), compressed (to ~56 kbps), and stored on a flash-RAM hard drive (~200 MB per 8-h flight).

TABLE III
ANTENNA BEAM COUPLING COEFFICIENTS (η) BEFORE AND AFTER MARCH 15, 1999 TUNING

No.	Frequency (GHz)	Laboratory Measurements				After March 15, 1999 Tuning			
		η_Z^A	η_N^A	η_Z^H	η_N^H	η_Z^A	η_N^A	η_Z^H	η_N^H
1	50.30	0.0048	0.0016	0.0057	0.0014	0.0055	0.0017	0.0086	0.0024
2	51.76	0.0066	0.0021	0.0053	0.0014	0.0066	0.0021	0.0071	0.0020
3	52.80	0.0077	0.0024	0.0054	0.0013	0.0093	0.0023	0.0023	0.0010
4	53.75	0.0071	0.0024	0.0045	0.0014	0.0141	0.0024	0.0089	0.0026
5	54.40	0.0073	0.0023	0.0050	0.0016	0.0084	0.0024	0.0010	0.0010
6	54.94	0.0082	0.0027	0.0056	0.0018	0.0092	0.0028	0.0012	0.0010
7	55.50	0.0107	0.0031	0.0080	0.0023	0.0091	0.0029	0.0025	0.0010
8	56.02	0.0163	0.0044	0.0129	0.0034	0.0101	0.0032	0.0010	0.0010

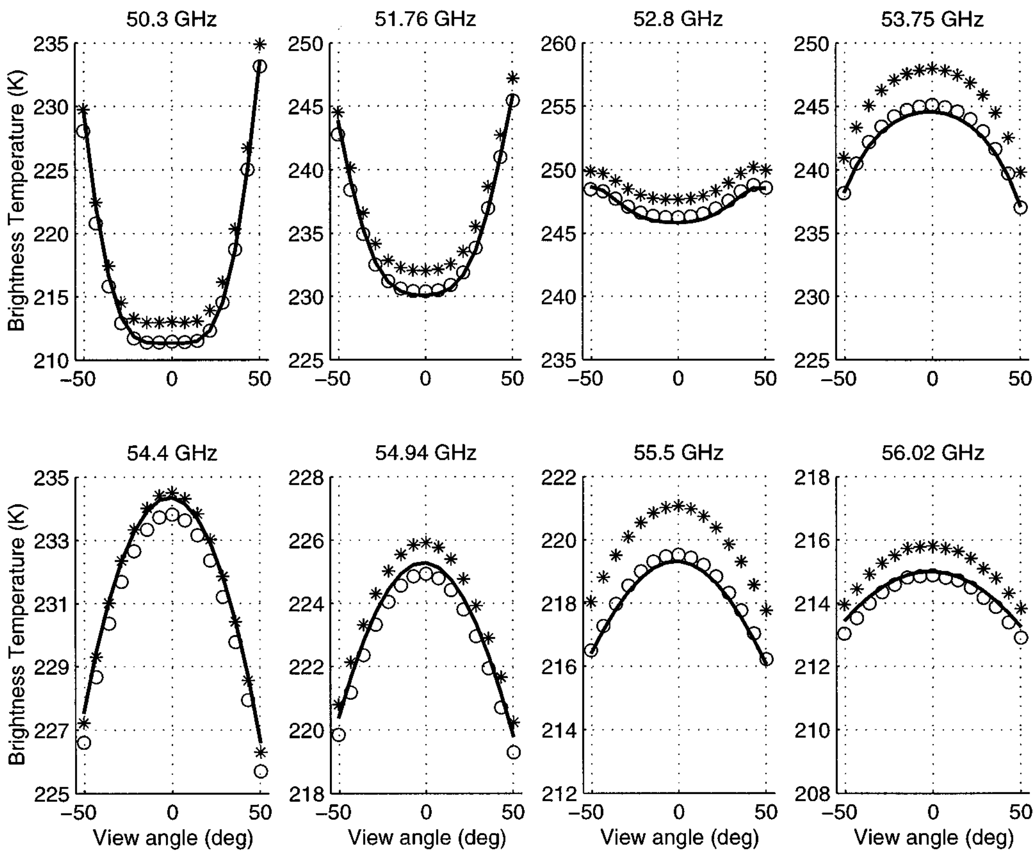

Fig. 5. Comparison of NAST-M 54-GHz channels with AMSU (March 26, 1999 overpass, 00:41 UTC). Brightness temperatures calculated from AMSU radiances are shown with a solid line, and NAST-M radiances (corrected for antenna beam spillover) are shown with circles. NAST-M radiances before spillover corrections have been applied and are indicated with asterisks.

III. CALIBRATION AND VALIDATION

The radiometer output voltage C for each channel is converted into units of brightness temperature T_B by the application of the linear calibration equation

$$T_B(C) = gC + b = [g\ b] \cdot \begin{bmatrix} C \\ 1 \end{bmatrix} \equiv \mathbf{x}^T \mathbf{c}. \tag{1}$$

We use bold lowercase letters to denote vectors and $(\cdot)^T$ to denote the transpose operator. The gain (g) and baseline (b) represented by the vector $\mathbf{x}$ are derived by fitting a line to the three calibration points (C_Z, T_Z), (C_A, T_A) and (C_H, T_H), where the subscripts Z, A, and H indicate the zenith, ambient, and heated calibration sources, respectively. The parameters of the linear fit are determined by weighted least-squares

$$\mathbf{x} = (\mathbf{A}^T\mathbf{W}\mathbf{A})^{-1}\mathbf{A}^T\mathbf{W}\mathbf{b}$$
$$\mathbf{A}^T = \begin{bmatrix} C_Z & C_A & C_H \\ 1 & 1 & 1 \end{bmatrix} \quad \mathbf{b} = [T_A \quad T_A \quad T_H]^T$$
$$\mathbf{W} = \begin{bmatrix} \sigma_Z & 0 & 0 \\ 0 & \sigma_A & 0 \\ 0 & 0 & \sigma_H \end{bmatrix}^{-2}. \tag{2}$$

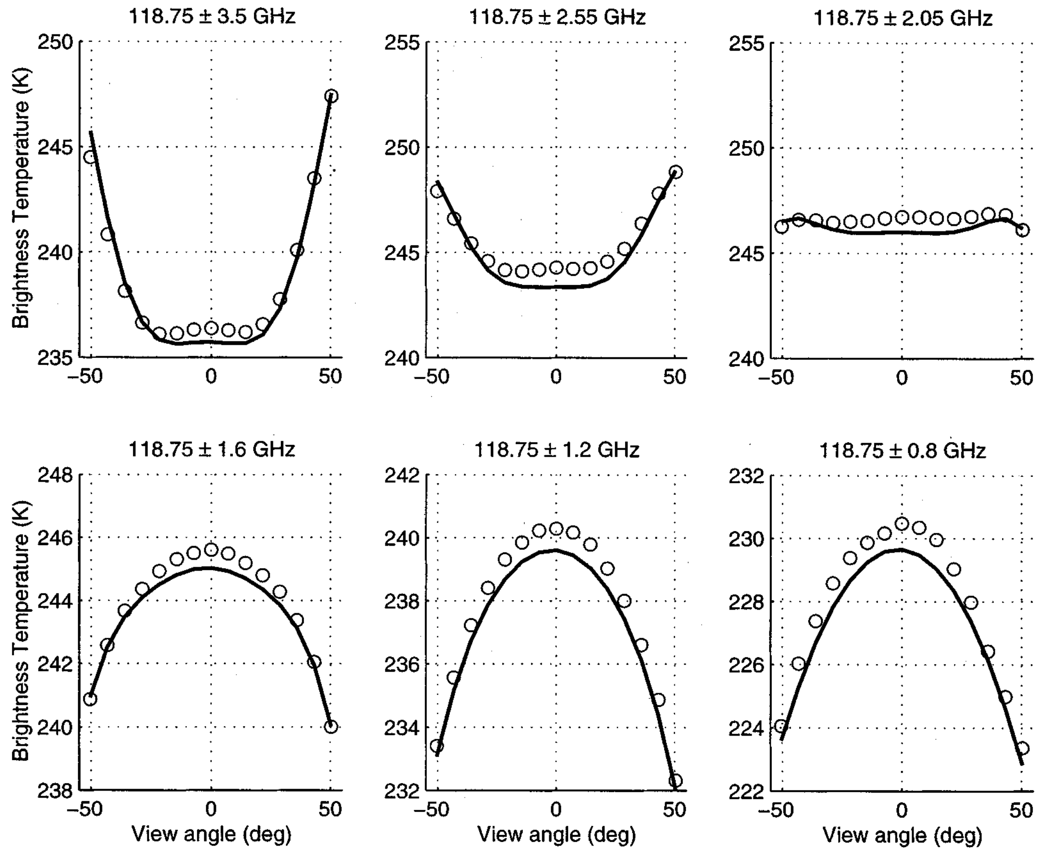

Fig. 6. Comparison of NAST-M 118-GHz channels with AMSU (March 26, 1999 overpass, 00:41 UTC). Brightness temperatures calculated from AMSU radiances are shown with a solid line, and NAST-M radiances are shown with circles.

The $\mathbf{W}$ matrix is the inverse of the error covariance of the calibration data and includes contributions due to instrument noise (see Table I), unknown thermal gradients in the internal targets, and, for the 54-GHz system, antenna beam spillover. The latter two contributions are discussed in more detail in Section III. The calibration counts C_H and C_A are typically filtered over several scans to reduce sensor noise using methods such as described in [9].

A. Correction for Thermal Gradients in the Heated Target

Temperature sensors embedded throughout the heated and ambient targets allow detection of thermal gradients, both across and through the load. These must be measured at high altitudes because the low air pressure and temperature are difficult to replicate on the ground, as is the impact of this gradient on the load radiance at each frequency. Measurements of the ambient target temperature have indicated a worst-case gradient of ± 0.1 K. Therefore, no correction is required. Temperature differences through the heated target as large as 3 K have been observed, and correction is necessary. It is assumed that the brightness temperature T_B^H observed while viewing the heated target is a weighted average of the temperatures $\mathbf{T_H}$ measured by the seven embedded sensors

$$T_B^H = \mathbf{w}^T \mathbf{T_H}, \quad \text{where} \quad \sum_{i=1}^{7} w(i) = 1. \tag{3}$$

Radiometric measurements at 118.75 ± 3.5 GHz of the ambient target and the cosmic background (known to within ± 0.1 K) are used as calibration points for determining the brightness temperature of the heated target. The solution to (3) is chosen such that $\sum w^2$ is minimized

$$\mathbf{w} = \begin{bmatrix} & & & \mathbf{T_H^T} & & & \\ 1 & 1 & 1 & 1 & 1 & 1 & 1 \end{bmatrix}^+ \cdot \begin{bmatrix} T_B^H \\ 1 \end{bmatrix} \tag{4}$$

where $(\cdot)^+$ denotes the pseudo-inverse. These weights are typically calculated for each 54- and 118-GHz channel using only the 118.75 ± 3.5 GHz channel for calibration. Because the penetration depth into the load is frequency-dependent, the weights are also frequency-dependent, but this dependence has been found to be negligible (on the order of ± 0.1 K) for both radiometer systems. Note that by using the zenith and ambient calibration sources to correct the heated load at 118.75 ± 3.5 GHz, we have effectively replaced the three-point calibration with a two-point calibration for this channel. However, all other channels use a weighted average of all three calibration sources.

B. Characterization and Correction of Antenna Beam Spillover

An antenna beam spillover problem affecting views of the internal calibration targets for the 54-GHz radiometer results in a correctable worst-case absolute calibration bias of $\sim$3 K in the transparent channels. The "corrupted" temperature of the ambient/heated load can be modeled as a linear combination of the spillover through the zenith port, the spillover through the

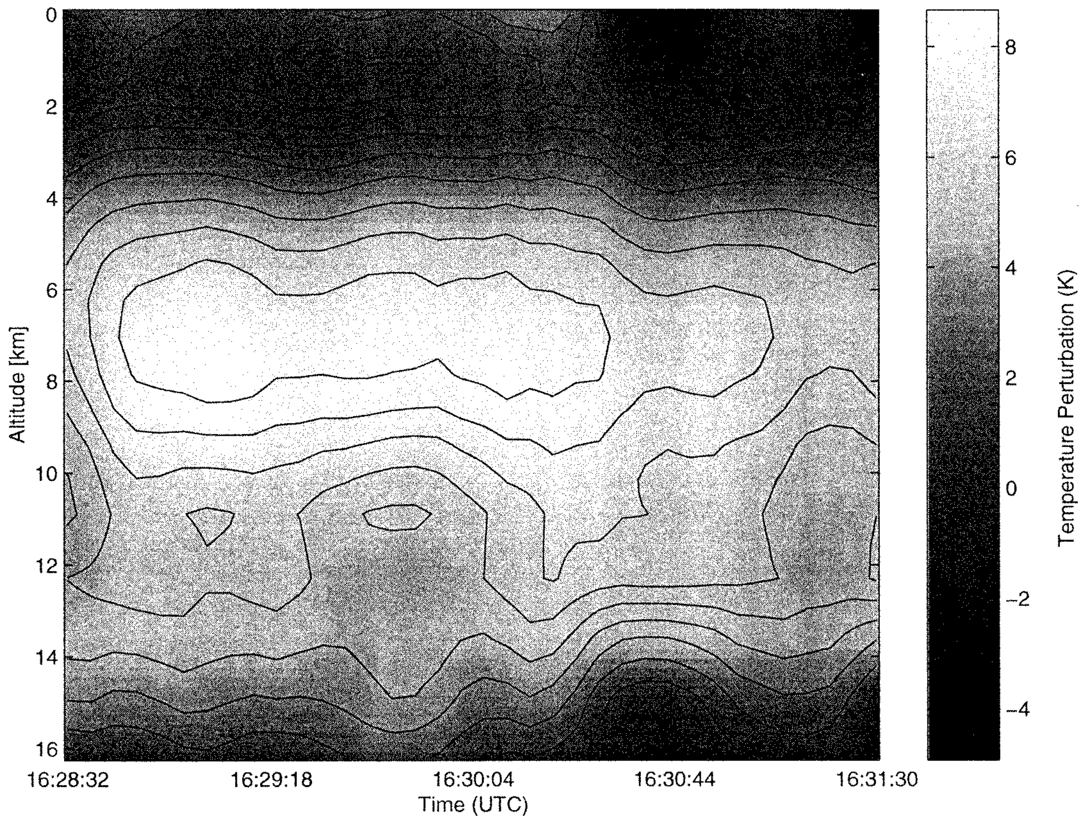

Fig. 7. Warm core temperature profile retrieval for the eye of Hurricane Bonnie, August 26, 1998, relative to clear air 180 km to the east. The horizontal extent of the retrieval is approximately 35 km. Contour lines are drawn for every 1 K change in retrieved temperature, with the warmest contour at 7.7 K.

nadir port, and the "true" load temperature (i.e., the brightness temperature [T_A or T_H] that would be observed if there were no spillover) as follows:

$$T'_A = \eta_Z^A T_Z + \eta_N^A T_N + (1 - \eta_Z^A - \eta_N^A) T_A \tag{5}$$

$$T'_H = \eta_Z^H T_Z + \eta_N^H T_N + (1 - \eta_Z^H - \eta_N^H) T_H. \tag{6}$$

The four η values (for each radiometer channel) can be accurately measured in the laboratory, T_Z and T_N can be estimated from flight data, and (5) and (6) can be substituted in (2) to provide a correction. The η values depend on the azimuthal and lateral position of the reflector relative to the motor shaft, and consequently need to be measured again if the reflector position relative to the motor shaft changes. Unfortunately, the NAST-M scanning assembly underwent numerous repairs over the course of CAMEX-3 and WINTEX that affected the reflector position relative to the motor shaft, and the laboratory measurements of the values were no longer applicable.

However, lab-derived measurements of the η values can be "tuned" for flight observations by comparing calibrated NAST-M data to radiosonde (or AMSU) data. Specifically, let T_B^U and T_B^D represent upwelling and downwelling brightness temperatures calculated from radiosonde data for a particular NAST-M channel. Let $\overline{T_B^U}$ and $\overline{T_B^D}$ represent NAST-M calibrated (using only ambient and heated targets) brightness temperatures (using lab-derived ηs) when viewing the nadir and zenith positions, respectively. The tuned values of η are the solutions to the following constrained minimization problem:

$$\text{minimize } (\boldsymbol{\eta} - \boldsymbol{\eta}_o)^T (\boldsymbol{\eta} - \boldsymbol{\eta}_o) \text{ subject to} \tag{7a}$$

$$\boldsymbol{\eta}^T \geq [0.001 \quad 0.001 \quad 0.001 \quad 0.001] \tag{7b}$$

$$\left(\overline{T_B^U} - T_B^U\right)^2 \leq \varepsilon_U^2 \tag{7c}$$

$$\left(\overline{T_B^D} - T_B^D\right)^2 \leq \varepsilon_D^2. \tag{7d}$$

where $\boldsymbol{\eta}_o$ is the vector of laboratory measurements. The error terms ε_U^2 and ε_D^2 include contributions due to instrument noise (see Table I), profile error (assumed to be less than ± 1 K for radiosonde observations and AMSU at NAST-M vertical resolution), and forward model error (assumed to be less than ± 0.3 K). The minimization is carried out numerically using a sequential quadratic programming (SQP) method [10]. Laboratory measurements of the parameters before and after a March 15, 1999 tuning appear in Table III.

C. Comparisons With AMSU

NAST-M radiances observed on March 26, 1999 over Lake Michigan were compared with radiances observed by AMSU in the following way. First, a temperature retrieval was performed using the AMSU-A channels [11]. A humidity profile was obtained using data from a coincident radiosonde, and the surface temperature was retrieved using the 11-μm and 12-μm channels from the Advanced Very-High Resolution Radiometer (AVHRR) on the NOAA-15 satellite. These data were used with a forward model [12] and a sea-surface model [13] to simu-

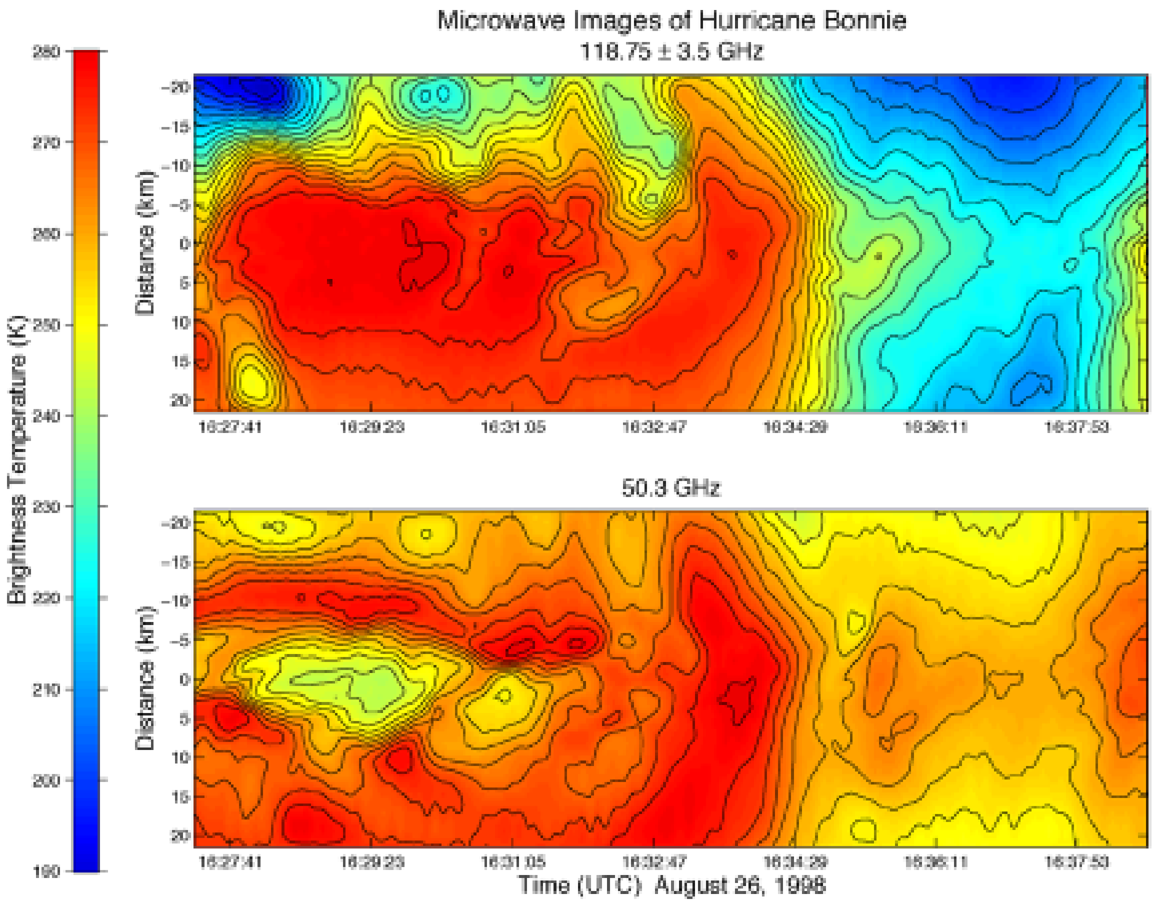

Fig. 8. Brightness temperature images over the eye of Hurricane Bonnie, August 26, 1998, at window frequencies near 50.3 GHz and 118.75 ± 3.5 GHz. The contour spacing is 5 K below 240 K and 4 K above. The x–y scales are equal at 10-km altitude, where the image size is approximately 40 km × 140 km.

late NAST-M radiances for viewing angles ±50° from nadir. Simulated brightness temperatures were band-averaged over the NAST-M passbands using laboratory measurements of the radiometer frequency response over 1200 frequencies. A Gaussian antenna beamshape was assumed in the radiative transfer calculations, as suggested by [14]. The errors associated with the simulated NAST-M brightness temperatures due to AMSU calibration/retrieval errors [11], [15], forward model errors [16], surface emissivity model errors [13], AVHRR calibration/retrieval errors [17], and temporal and spatial offsets are believed to be less than 1.5 K for all channels. Corrections for antenna sidelobe spillover affecting the 54-GHz system were derived from a March 15, 1999 overflight of Lake Michigan using temperature and humidity profiles retrieved from AMSU and surface temperature data from buoy station 45007 (NOAA National Data Buoy Center). The results are shown in Figs. 5 and 6. Channels 7–9 of the 118-GHz system are significantly degraded due to RF losses in the preamplifier circuits, and are not shown. The brightness temperatures calculated from AMSU radiances are shown with a solid line, and NAST-M radiances (averaged from 00:36–00:44 UTC; straight and level flight over water) are shown with circles. NAST-M brightness temperatures near 54 GHz before spillover corrections are indicated with asterisks. Agreement to within 1 K is obtained for all channels of the 54-GHz radiometer and channels 1–6 of the 118-GHz radiometer. AMSU/AVHRR/NAST-M comparisons on March 29, 1999 over Lake Michigan demonstrate similar agreement.

The excellent agreement between NAST-M and AMSU, while encouraging, is only indicative of the calibration of NAST-M relative to AMSU. More extensive studies are needed in order to validate the absolute calibration accuracy of NAST-M under all circumstances.

IV. Observations of Thermal and Precipitation Structure in Hurricane Bonnie (August 26, 1998)

The eight temperature sounding channels near 54 GHz and the six near 118 GHz were used as inputs to a neural network to retrieve temperature profiles. A training ensemble of 500 radiosondes (< ±45° latitude) selected from the TIGR profile set [18] were used with the forward and sea–surface models described in Section III-C to produce simulated brightness temperatures at the NAST-M frequencies. Temperatures were retrieved along-track (nadir only) at 22 levels ranging from 0 to 16 km. The retrievals were filtered (in the along-track direction only) with a triangular filter of length five and were then bilinearly interpolated by a factor of two in the vertical and along-track directions. Fig. 7 illustrates the difference between the temperature profile retrieved by NAST-M near nadir as it crossed the eye of Hurricane Bonnie on August 26, 1998 near 16:30 UTC, and the temperature profile observed a few minutes earlier in relatively clear air 180 km to the east. The warm core aloft appears to peak near 8 K at altitudes between 5 and 10 km. The magnitude and form of hurricane warm cores are well-known indicators of wind

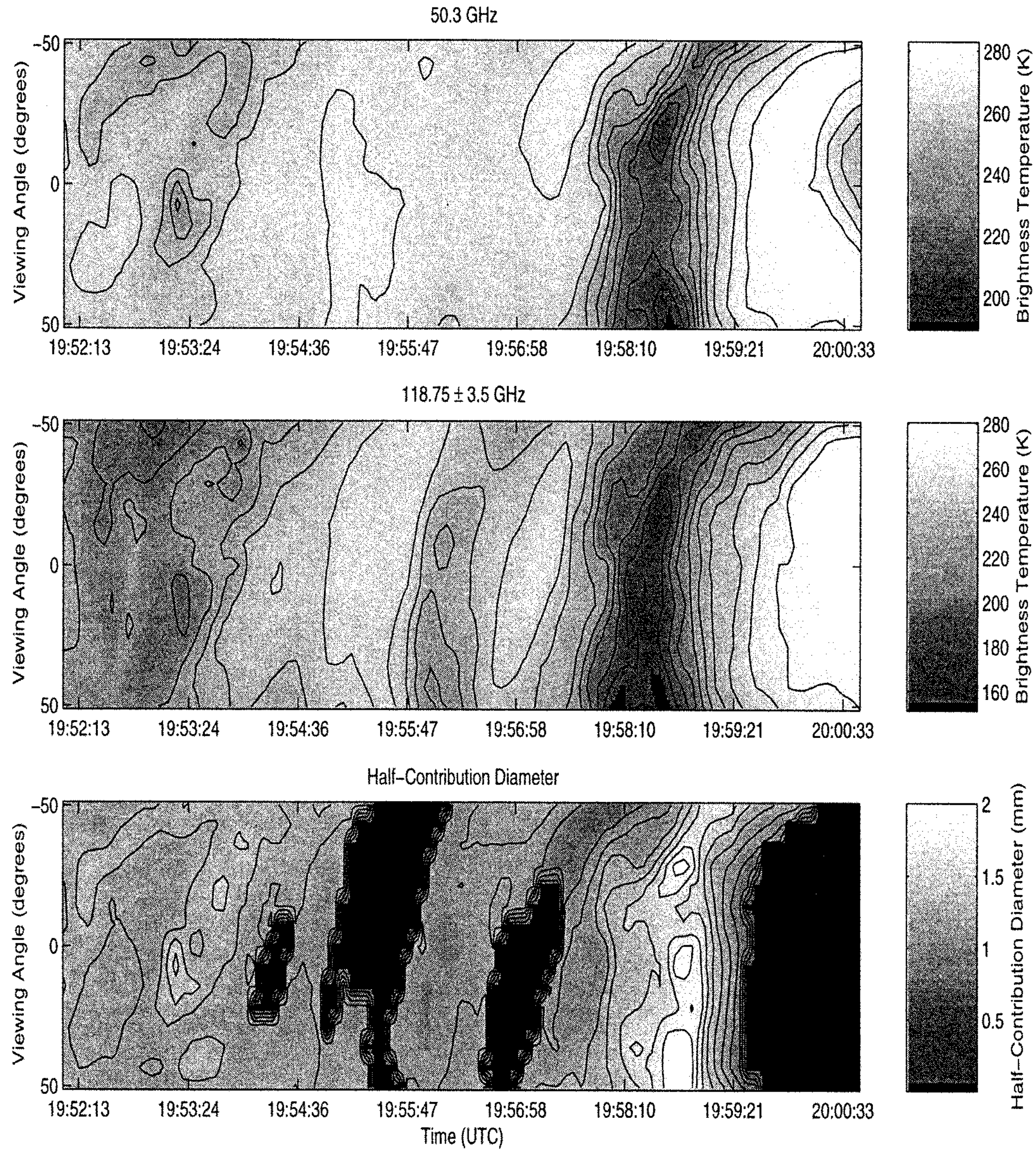

Fig. 9. NAST-M observations of one eyewall and two rainbands of Hurricane Bonnie, August 23, 1998. (a) Radiance image near 50.3 GHz (contour lines every 10 K, warmest contour at 273.5 K), (b) radiance image near GHz (contour lines every 15 K, warmest contour at 267.5 K), and (c) retrieved particle size index (contour lines every 0.2 mm, largest contour at 1.8 mm); larger values correspond to larger particles (see Fig. 10).

speed and structure of hurricanes and have been used to monitor hurricane strength [6], [19]–[21]. Fig. 8 presents the brightness temperature images observed in the window channels associated with the 54- and 118-GHz radiometers. The lower brightness temperatures observed in the center of the eye near 50 GHz result partly from the reflection of cold space from the ocean surface, whereas such surface effects are largely absent near 118 GHz because of the greater absorption there by tropospheric water vapor. The cold temperatures observed near 118 GHz (upper left of the top image) arise due to scattering of cold space off hydrometeors in a rain band on the edge of the hurricane eye. A band of moist air or cloud crosses the eye near 16:30 UTC.

The combination of 54- and 118-GHz spectral data reveals information about hydrometeor size distributions and cell-top altitudes, and about the correlated parameters, vertical wind velocity, and precipitation rate. Precipitation increases directly with the vertical velocity of saturated air into cold condensing regions, provided we neglect re-evaporation at lower altitudes. Fig. 9(a) illustrates how such spectral data reveals precipitation structure. This figure shows a narrow cold band near 50.3 GHz that corresponds to higher precipitation rates in the eyewall of Hurricane Bonnie on August 23, 1998, while Fig. 9(b) also highlights smaller hydrometeors that delineate the broader (cold) rain bands visible near 118.75 $\pm$ 3.5 GHz from 19:52–19:53 and 19:56 UTC.

From such data it is difficult to retrieve separately precipitation parameters such as rain rate, drop size, cell-top altitude, and cloud density because they are highly correlated. For example, high vertical winds will generally increase the rate of condensation, support larger drops aloft, push to higher altitudes, and result in greater cloud densities. Nonetheless, certain trends in the distinctive effects of these various parameters are evident in radiative transfer calculations based on simple cloud models. Fig. 10 suggests how spectral differences between the 54- and 118-GHz oxygen absorption bands can reveal information about hydrometeor sizes and cell-top altitudes. The distribution of lower bright-

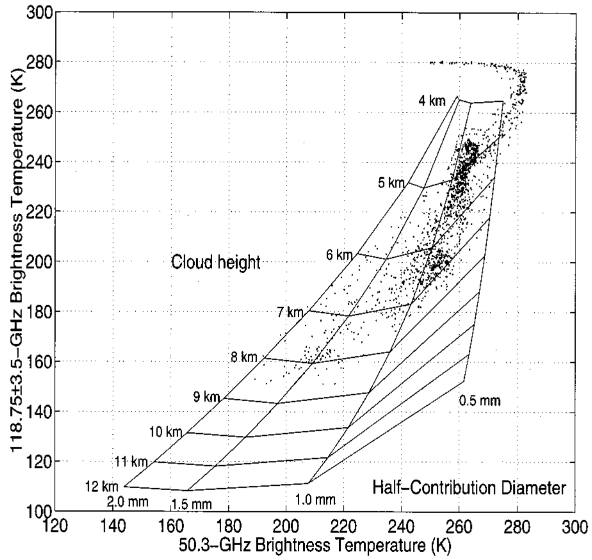

Fig. 10. Relative radiances observed over Hurricane Bonnie, August 23, 1998 near 50.3 GHz and 118.75 $\pm$ 3.5 GHz, illustrating the nominal effects of particle size and the definition of the size metric illustrated in Fig. 9(c).

ness temperatures extending downwards and to the left results from greater numbers of larger hydrometeors aloft at higher altitudes, and therefore generally greater precipitation rates. Observation offsets orthogonal to this reference direction "z" provide additional information. For example, the cloud model presented by Gasiewski and Staelin [22] exhibited iso-altitude contour lines in the 53.65/118.75 $\pm$ 1.45 GHz plane that were generally oriented between the z and horizontal axes.

A similar set of theoretical contours is overlaid on Fig. 10 based on a tropical standard atmosphere with 1 g/m^3 water (ice, below 0 °C) in spherical drops having exponentially distributed diameters from the surface up to a variable cloud top altitude. The contours are labeled with median mass-weighted drop diameters (half the mass is in larger drops) and cell-top altitudes. The contour lines associated with constant drop size are generally oriented between the z and vertical axes and closer to z, with larger drops corresponding to colder 50.3-GHz brightness temperatures. These same contours applied to the data of Fig. 9(a) and (b) yield the inferred-drop-size image shown in Fig. 9(c), which suggests that the largest particles are found toward the inner edge of the hurricane eyewall, consistent with stronger convection there. No diameters are presented for inferred cell-top altitudes below 4.9 km. Particle diameter is only one of the links between spectral observations and precipitation rates; others include cell-top altitude, absolute albedo, and the adjacent temperature and humidity profiles. Further treatment of these retrieval issues requires additional modeling and data, and are being pursued separately.

V. Discussion

NAST-M offers several noteworthy improvements over most prior aircraft and satellite-based instruments, as discussed in the following.

The zenith port provides 1) an additional highly stable calibration source for the more transparent channels, 2) a mechanism for measuring and compensating a thermal gradient in the heated target (thereby improving the calibration of the more opaque channels), and 3) a source of data for validating transmittance models.

The use of commercial off-the-shelf (COTS) components dramatically reduced development time and cost. Thermal and mechanical environments throughout the instrument housing were engineered to ensure reliability of COTS hardware. NAST-M was designed, developed, and flown in under two years at a cost under \$800 000.

NAST-M provides the first high-resolution, co-located, multiband passive microwave measurements for three-dimensional (3-D) temperature sounding, cloud and precipitation studies, and transmittance modeling. NAST-I/M provides an atmospheric sounding platform with sufficient accuracy and sensitivity for validating satellite observation system concepts. The 2.6-km resolution provided by the NAST suite also facilitates interpretation of unresolved satellite observations of meteorological phenomena.

VI. Summary and Conclusions

The three-point calibration on NAST-M provides accurate brightness temperature measurements in two oxygen bands, permitting the first reliably accurate temperature profile retrieval images. The utility of dual-absorption band measurements for characterization of convective precipitation is illustrated by observations of rainbands in Hurricane Bonnie. The ER-2 platform provided high spatial resolution of this storm"s structure, including its warm core. Future development of NAST-M will include addition of radiometer subsystems for higher frequency bands.

Acknowledgment

The authors wish to thank the NASA-Dryden ER-2 pilots and ground crew and personnel associated with CAMEX-3 and WINTEX for their support and assistance, D. Bold and D. Cousins of MIT Lincoln Laboratory, Lexington, MA, for their help with the development of NAST-M instrument hardware, S. Mango of the Integrated Program Office for his support of the NAST development program, and the anonymous reviewers for many helpful comments.

References

[1] D. Cousins and W. L. Smith, "NPOESS airborne sounder testbed—Interferometer," in *Proc. Engineering and Instrumentation Symp.*, San Diego, CA, Aug. 1997.

[2] A. J. Gasiewski, J. W. Barrett, P. G. Bonanni, and D. H. Staelin, "Aircraft-based radiometric imaging of tropospheric temperature and precipitation using the 118.75-GHz oxygen resonance," *J. Appl. Meteorol.*, vol. 29, pp. 620–632, July 1990.

[3] M. S. Spina, M. J. Schwartz, D. H. Staelin, and A. J. Gasiewski, "Application of multilayer feedforward neural networks to precipitation cell-top estimation," *IEEE Trans. Geosci. Remote Sensing*, vol. 36, pp. 154–162, Jan. 1998.

[4] M. J. Schwartz, J. W. Barrett, P. W. Fieguth, P. W. Rosenkranz, M. S. Spina, and D. H. Staelin, "Observations of thermal and precipitation structure in a tropical cyclone by means of passive microwave imagery near 118 GHz," *J. Appl. Meteorol.*, vol. 35, pp. 671–678, May 1996.

[5] A. J. Gasiewski and D. H. Staelin, "Statistical precipitation cell parameter estimation using passive 118-GHz O_2 observations," *J. Geophys. Res.*, vol. 94, pp. 18 367–18 378, 1989.

[6] D. H. Staelin and F. W. Chen, "Precipitation observations near 54 and 183 GHz using the NOAA-15 satellite," *IEEE Trans. Geosci. Remote Sensing*, vol. 38, pp. 2322–2332, Sept. 2000.
[7] R. V. Leslie, "Temperature profile retrievals with the NAST-M passive microwave spectrometer,", S.M. thesis, Mass. Inst. Technol., Cambridge, MA, 2000.
[8] M. Barabanov and V. Yodaiken, "Real-time Linux," *Linux J.*, Mar. 1996.
[9] G. E. Peckham, "An optimum calibration procedure for radiometers," *Int. J. Remote Sensing*, vol. 10, pp. 227–236, 1989.
[10] P. E. Gill, W. Murray, and M. H. Wright, *Practical Optimization*. London, U.K.: Academic, 1981.
[11] P. W. Rosenkranz, "Retrieval of water vapor from AMSU-A and AMSU-B measurements," *IEEE Trans. Geosci. Remote Sensing*, vol. 39, pp. 2429–2435, Nov. 2001.
[12] ——, "Absorption of microwaves by atmospheric gases," in *Atmospheric Remote Sensing by Microwave Radiometry*, M. A. Janssen, Ed. New York: Wiley, 1993, ch. 2.
[13] K. Lamkaouchi, E. Berge, and W. Ellison, "New permittivity data for sea water (30–100 GHz)," ESA, ESA report 11 197/94/NL/CD, Noordwijk, The Netherlands, 1997.
[14] H. F. Teh, "Development and use of an antenna gain pattern test system for the NAST-M microwave radiometer at ∼54 GHz,", M.Eng. thesis, Mass. Inst. Technol., Cambridge, 2001.
[15] T. Mo, "Prelaunch calibration of the advanced microwave sounding unit-A for NOAA-K," *IEEE Trans. Microwave Theory Tech.*, vol. 44, pp. 1460–1469, 1996.
[16] M. J. Schwartz, "Observation and modeling of atmospheric oxygen millimeter-wave transmittance," Ph.D. dissertation, Mass. Inst. Technol., Cambridge, 1998.
[17] D. J. Schwab, G. A. Leshkevich, and G. C. Muhr, "Satellite measurements of surface water temperature in the Great Lakes—Great Lakes CoastWatch," *J. Great Lakes Res.*, vol. 18, no. 2, pp. 247–258, 1992.
[18] A. Chedin, N. A. Scott, C. Wahiche, and P. Moulinier, "The improved initialization inversion method: A high-resolution physical method for temperature retrievals from the TIROS-N series," *J. Clim. Appl. Meteorol.*, vol. 24, pp. 128–143, 1985.
[19] N. C. Grody, C. M. Hayden, W. C. C. Shen, P. W. Rosenkranz, and D. H. Staelin, "Typhoon June winds estimated from scanning microwave spectrometer measurements at 55.45 GHz," *J. Geophys. Res.*, vol. 84, pp. 3689–3695, 1979.
[20] C. S. Velden, "Observational analyses of North Atlantic tropical cyclones from NOAA polar-orbiting satellite microwave data," *J. Appl. Meteorol.*, vol. 28, pp. 59–70, 1989.
[21] S. Q. Kidder *et al.*, "Satellite analysis of tropical cyclones using the Advanced Microwave Sounding Unit (AMSU)," *Bull. AMS*, vol. 101, no. 6, pp. 1241–1259, 2000.
[22] A. J. Gasiewski and D. H. Staelin, "Numerical modeling of passive microwave O_2 observations over precipitation," *Radio Sci.*, vol. 25, no. 3, pp. 217–235, 1990.

William J. Blackwell (S'92) received the B.S. degree in electrical engineering from the Georgia Institute of Technology, Atlanta, in 1994, and the S.M. degree in electrical engineering from the Massachusetts Institute of Technology (MIT), Cambridge, in 1995. He is currently pursuing the Ph.D. degree at the Research Laboratory of Electronics, MIT.

His research interests are in the areas of atmospheric remote sensing and estimation and signal processing theory.

Mr. Blackwell held a National Science Foundation Graduate Research Fellowship from 1994 to 1997 and is a member of Tau Beta Pi, Eta Kappa Nu, Phi Kappa Phi, and Sigma Xi.

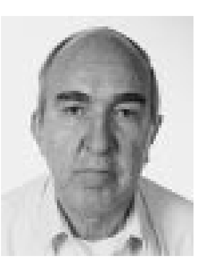

John W. Barrett, has been a Member of Technical Staff at the MIT Research Laboratory of Electronics, Cambridge, since 1951, and the Harvard-Smithsonian Center for Astrophysics, Cambridge, since 1988. He has been involved with the design, fabrication, and deployment of many ground-based, airborne, and balloonborne atmospheric sensors.

Frederick W. Chen (S'97) received the S.B. and the M.Eng. degrees in electrical engineering from the Massachusetts Institute of Technology (MIT), Cambridge, MA, in 1998, where he is currently pursuing the Ph.D. degree.

From May to August of 1996, he participated in the Summer Research Participation Program, Argonne National Laboratory, Argonne, IL, where he worked in the Reactor Analysis Division on machine condition monitoring using maximum likelihood estimation and neural nets. Since June 1997, he has been with the Remote Sensing and Estimation Group, MIT Research Laboratory of Electronics, studying methods for estimating precipitation rates from passive microwave spectrometers on meteorological satellites and aircraft.

R. Vincent Leslie (S'96) received the B.S. degree in electrical engineering from Boston University, Boston, MA, in 1998, and the S.M. degree in electrical engineering from the Massachusetts Institute of Technology (MIT), in 2000, where he is currently pursuing the Sc.D. degree.

He is currently a Research Assistant for the Remote Sensing and Estimation Group, Research Laboratory of Electronics, where he is studying potential applications of new science in remote sensing satellites. He interned at the Raytheon Electronic Systems' Missile Radar Laboratory, Tewksbury, MA.

Dr. Leslie is a member of Tau Beta Pi and The Order of the Engineer.

Philip W. Rosenkranz (S'68–M'71–SM'84–F'97) received the S.B., S.M., and Ph.D. degrees in electrical engineering from the Massachusetts Institute of Technology in 1967, 1968, and 1971, respectively.

He did postdoctoral work at Caltech's Jet Propulsion Laboratory, then in 1973 joined the Research Staff at M.I.T.'s Research Laboratory of Electronics, where he is presently a Principal Research Scientist. His field of interest is the interaction of electromagnetic waves with constituents of the terrestrial atmosphere and surface, and remote sensing of geophysical parameters from aircraft and satellites. Examples of this work are theoretical models for absorption in molecular oxygen and water vapor, and studies of hurricane phenomenology, such as the warm core and scattering in rainbands, with microwave radiometers. He is a member of the Science Team for the Atmospheric Infrared Sounder Facility on NASA's Earth Observing System.

Michael J. Schwartz attended Deep Springs College, Deep Springs, CA, and received the B.A. degree in physics from Carleton College, Northfield, MN, in 1985, and the Ph.D. degree in physics from Massachusetts Institute of Technology (MIT), Cambridge, in 1988.

He was a Staff Scientist in the MIT Research Laboratory of Electronics from 1997 to 1998, contributing to the development and operation of an aircraft-based millimeter-wave sounder, NAST-M. He joined the Microwave Atmospheric Science Team, Jet Propulsion Laboratory, Pasadena, CA, in 1999. He is currently involved in the development of the Earth Observing System (EOS) Microwave Limb Sounder (MLS), which is to launch on the EOS AURA satellite.

David H. Staelin (S'59–M'65–SM'75–F'79) received the B.S., M.S., and Sc.D. degrees in electrical engineering from the Massachusetts Institute of Technology (MIT), Cambridge, in 1960, 1961, and 1965, respectively.

He joined the MIT Faculty in 1965, where he is Professor of Electrical Engineering and Assistant Director of the Lincoln Laboratory. He teaches electromagnetics and signal processing. He was Principal Investigator for the NEMS and SCAMS microwave spectrometer experiments on the NASA Nimbus-5 and the Nimbus-6 satellites and a Co-Investigator for the NASA AIRS/AMSU/HSB sounding experiment on Aqua, for EOS, the SMMR microwave experiment on Nimbus 7, and the Planetary Radio Astronomy Experiment on Voyager 1 and 2. Other research has involved radio astronomy, video coding, milliarc-second optical astrometry, and random process characterization.

NPOESS Aircraft Sounder Testbed-Microwave: Observations of Clouds and Precipitation at 54, 118, 183, and 425 GHz

R. Vincent Leslie, *Student Member, IEEE* and David H. Staelin, *Fellow, IEEE*

***Abstract*—The National Polar-orbiting Operational Environmental Satellite System (NPOESS) Aircraft Sounder Testbed—Microwave (NAST-M) includes spectrometers operating near the oxygen lines at 50–57, 118.75, and 424.76 GHz, and a spectrometer centered on the water vapor absorption line at 183.31 GHz. All four of the spectrometers' antenna horns are collocated, have 3-dB (full-width at half-maximum) beamwidths of 7.5°, and are directed at a single mirror that scans cross-track beneath the aircraft with a swath up to 100-km wide. The first part of the paper describes the instrumentation and calibration for the newly installed spectrometers at 183.31 and 424.76 GHz. The second part demonstrates the potential performance of NAST-M, by presenting radiance images and precipitation rate and cell-top retrievals obtained during overflights of isolated convective storm cells, and by comparing these results with coincident visible images. NAST-M radiances are also compared with visible, infrared, and radar images. The nonlinear retrieval method was trained with a simple precipitation model. The data were obtained during the Cirrus Regional Study of Tropical Anvils and Cirrus Layers-Florida Area Cirrus Experiment (CRYSTAL-FACE 2002) and the Pacific THOR*pex* (THe Observing-system Research and *p*redictability *ex*periment) Observing System Test (PTOST 2003).**

***Index Terms*—Microwave images, microwave radiometry, microwave spectrum, millimeter-wave images, precipitation.**

I. Introduction

The National Polar-orbiting Operational Environmental Satellite System (NPOESS) Aircraft Sounder Testbed–Microwave (NAST-M) instrument consists of four independent total-power microwave spectrometers that share a scanning reflector. The original suite had two spectrometers near the oxygen lines at 50–57 GHz and the oxygen line at 118.75 GHz [1]. The two new spectrometers are double-sideband superheterodyne systems, one centered on the 183.31-GHz water vapor absorption line (183-GHz system) and the other centered on the 424.76-GHz oxygen absorption line (425-GHz system).

The original NAST-M suite has been used in a variety of remote sensing applications, including atmospheric profile retrievals (e.g., temperature [2]), cloud-parameter estimation (e.g., precipitation cloud-top altitude [3]), and cloud-clearing of coincident infrared data [4].

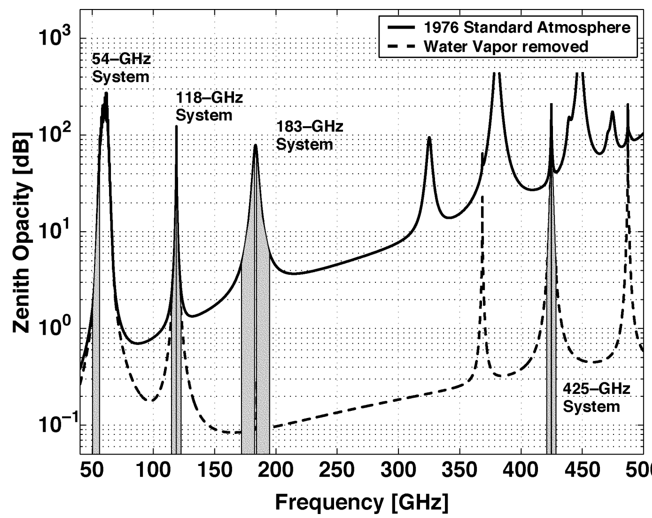

Fig. 1. Zenith opacity with overlapping NAST-M spectral coverage.

Passive microwave retrievals of temperature and water vapor profiles involve measurements of brightness temperatures near known absorption lines of oxygen and water vapor molecules. Fig. 1 shows the zenith opacity due to oxygen, nitrogen, and water vapor as a function of frequency; the NAST-M spectral coverage is overlaid. Zenith opacity is the integrated atmospheric attenuation from the terrestrial surface to the top of the atmosphere. For this simulation, the U.S. 1976 standard atmosphere was used with the Millimeter-wave Propagation Model [MPM] [5]. Hydrometeors (e.g., rain) both absorb and scatter electromagnetic waves.

The NAST-M spectrometer flies together with NAST-Interferometer (NAST-I), an 8500-channel infrared interferometric spectrometer scanning ±48.2° at wavelengths of 3.6–16.1 μm with 2.6-km resolution at an altitude of 20 km [6]. The NAST system is testing and validating measurement concepts essential to the success of the NPOESS global environmental satellite system. The new 183-GHz spectrometer, combined with the existing 50–57-GHz spectrometer, is validating concepts utilized by the Advanced Microwave Sounding Unit (AMSU) on the operational National Oceanic and Atmospheric Administration (NOAA) satellites, a precursor to the NPOESS Advanced Technology Microwave Spectrometer (ATMS) and the Conical scanning Microwave Imaging System (CMIS) planned for NPOESS

Manuscript received September 30, 2003; revised April 2, 2004. This work was supported in part by the U.S. Department of Commerce/National Oceanic and Atmospheric Administration under Contract DG133E-02-CN-0011 and in part by the National Aeronautics and Space Administration under Contract NAS5-31376.

R. V. Leslie is with the Lincoln Laboratory, Massachusetts Institute of Technology, Cambridge, MA 02420 USA.

D. H. Staelin is with the Research Laboratory of Electronics, Massachusetts Institute of Technology, Cambridge, MA 02139 USA (e-mail: staelin@mit.edu).

Digital Object Identifier 10.1109/TGRS.2004.834639

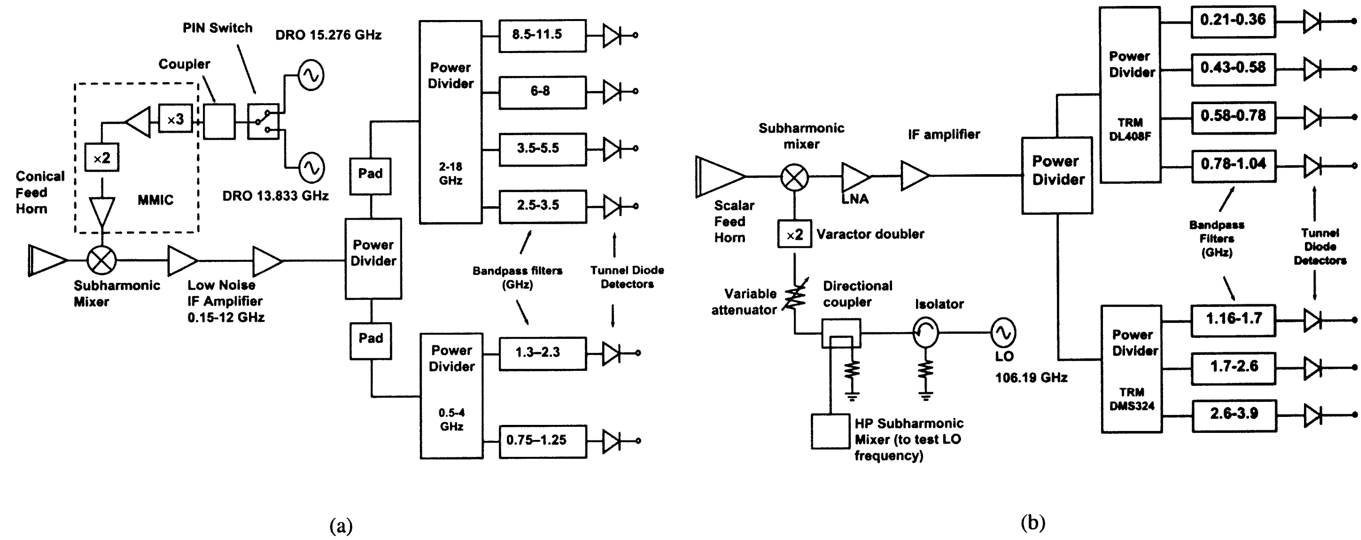

Fig. 2. Block diagrams of 183- and 425-GHz spectrometers. (a) 183-GHz spectrometer. (b) 425-GHz spectrometer.

(npoess.noaa.gov). The combination of the 183- and 425-GHz spectrometer data described in this paper provides preliminary validation of concepts proposed for utilization in future geostationary global-precipitation-monitoring satellites [7]. The critical advantage of these millimeter and submillimeter bands is their ability to yield spatial resolution comparable to ATMS and CMIS with geostationary antennas approximately 2–4 m in diameter.

The objective of this paper is to present the new spectrometers onboard the NAST-M suite and present the new potential of the combined spectrometers for precipitation parameter estimation.

II. Instrument Description

Initially, NAST-M was configured for the NASA ER-2 high-altitude airborne-science aircraft so that it could view both nadir and zenith. Late in 1999, the NAST-M suite was also integrated into the Proteus high-altitude aircraft, designed and built by Scaled Composites (Mojave, CA). The ER-2 has a maximum cruising altitude of 20 km, while Proteus cruises at 17 km. In Proteus, NAST-M flies in a pod underneath the fuselage and lacks the zenith view that it has on the ER-2's superpod. The loss of the zenith port reduces the three-point calibration, described in [1], to a two-point calibration, but also reduces leakage of zenith cold-space radiation into the antenna during calibration.

The spectrometers' four horns are directed at a single flat mirror, which scans cross-track beneath the aircraft with a swath width of ~100 km for altitudes of ~20 km. The 3-dB diameter of all four antenna beams is 7.5°, yielding a 2.6-km nadir footprint diameter from an altitude of 20 km. A single scan lasts approximately 5.5 s and includes views of three thermal calibration sources (two on the Proteus) and yields 19 spots across nadir from ±64.8° (Proteus from −54° to 68°). The most extreme ER-2 angles have footprints on the surface that are 14-km long in the crosstrack direction (e.g., see Fig. 4), and the extreme angles on each side of a scan are usually not included in NAST-M imagery because of excessive pixel size.

TABLE I
183- AND 425-GHz CHANNEL SPECIFICATIONS

183-GHz Spectrometer (LO = 183.31 GHz)			
No.	Frequency Offset (MHz)	Bandwidth (MHz)	Sensitivity (RMS K)
1	± 10000	3000	0.36
2	± 7000	2000	0.45
3	± 4500	2000	0.43
4	± 3000	1000	0.59
5	± 1800	1000	0.77
6	± 1000	500	1.39

425-GHz Spectrometer (LO = 424.76 GHz)			
No.	Frequency Offset (MHz)	Bandwidth (MHz)	Sensitivity (RMS K)
1	± 3250	1300	0.47
2	± 2150	900	0.52
3	± 1430	540	0.58
4	± 910	260	0.95
5	± 680	200	1.04
6	± 505	150	1.42
7	± 285	150	1.22

Channel specifications for the 183-GHz and 425-GHz spectrometers are given in Table I. Channel sensitivities were determined from actual aircraft data and include calibration noise. The nominal integration time for all spots (including calibration spots) is 100 ms. The block diagrams and channel specifications for the 54- and 118-GHz spectrometers were presented previously [1].

A. 183-GHz Spectrometer

A block diagram of the 183-GHz spectrometer system is shown in Fig. 2(a). A test-bench 183-GHz receiver was provided by Millitech's Millimeter-Wave Products Division (Northampton, MA). The receiver was then reconfigured and integrated into the NAST-M instrument so as to function in the harsh environmental conditions at 20-km altitude. The system was designed to switch between two local oscillators (LOs), but the second LO at 166 GHz was not operational. Bandpass filters define the spectrometer's temperature weighting functions, which are shown in Fig. 3 for all four spectrometers.

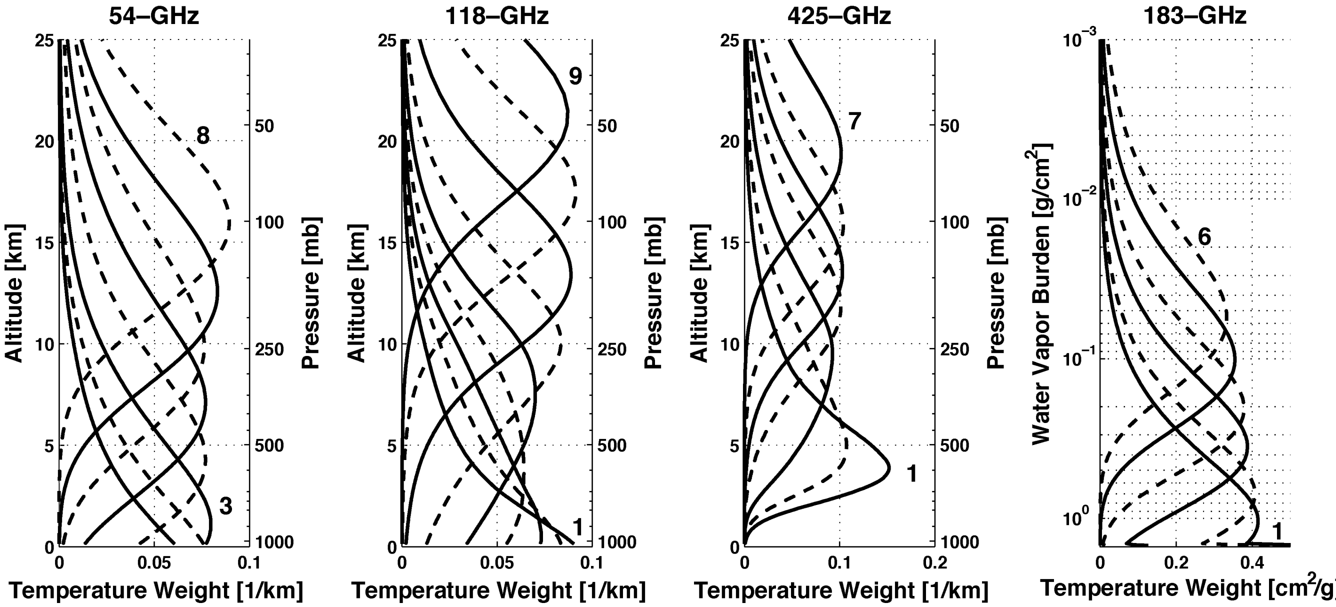

Fig. 3. Clear-air nadir temperature weighting functions for the U.S. 1976 standard atmosphere and a blackbody surface. Channel numbers can be related to frequencies through Table I. Note that the ER-2 cruises at 20 km and the Proteus at 17 km.

The 183-GHz weighting functions are plotted as a function of water vapor burden, a representation that is less dependent on the humidity profile. Water vapor burden is defined as the integrated water mass (grams per square centimeter) above a given altitude.

B. 425-GHz Spectrometer

A block diagram of the 425-GHz radiometer system is shown in Fig. 2(b). The receiver was designed and bench-tested at the University of Virginia and Virginia Diodes, Inc. (Charlottesville, VA) [8]. The Center for Space Research at the Massachusetts Institute of Technology designed and built the housing for the 425-GHz receiver. The LO for the 425-GHz receiver is a Gunn oscillator, which is temperature controlled to maintain its frequency. The Gunn is set to 106.19 GHz, and a varactor doubler upconverts the frequency, which then drives the subharmonic mixer. The 425-GHz receiver has a separate subharmonic mixer for measuring the LO frequency. Any deviations of the Gunn oscillator from the absorption line frequency cause the opaque temperature weighting functions to have two peaks instead of the desired bell shape.

Temperature weighting functions for the 425-GHz system are shown in Fig. 3. The 425-GHz channels furthest from the absorption line are sensitive to water vapor because of the water vapor continuum, and do not sense the surface. For example, channel 1 of the 425-GHz system has a weighting function very similar to channel four of the 183-GHz system, except that the 425-GHz channel is more sensitive to hydrometeors; it typically peaks near 4 km or 0.2 g/cm^2.

C. Calibration and Validation

Calibration consisted of laboratory experiments and comparisons between radiometric and simulated data. Laboratory measurements determined corrections to the temperatures of the onboard calibration loads, which were validated by measurements of a target submerged in liquid nitrogen. In a separate experiment, the optimal view-angle of the calibration loads was confirmed by rotating through all angles and choosing the angle with the maximum brightness temperature. Another experiment consisted of varying the 425-GHz LO frequency in simulations of the zenith-view brightness temperatures until the numerical simulations matched the actual flight data. From this test, it was determined that the 425-GHz LO frequency was 106.05 GHz and was off the absorption line by 0.56 GHz. This frequency shift was incorporated in the following validation simulations.

To validate the NAST-M calibration, dropsondes and radiosondes measured the temperature and humidity profiles in approximately the same area and time interval. These profiles were entered into a software program written to simulate brightness temperatures specifically for the NAST-M instrument; it used the Millimeter-wave Propagation Model [5]. These simulated brightness temperatures were then compared with the actual coincidental brightness temperatures measured by the instrument.

Fig. 4 is a flight map illustrating a typical profile comparison. The footprints of the radiometric data are plotted, and the footprints of the last scan are outlined in black. The footprints were projected from the altitude of the ER-2 to a flat surface, taking into account the scan angle. The dropsonde drop site is plotted, along with the trajectory of the dropsonde, as it fell from an altitude of 14 km. To supplement the atmospheric data above the dropsonde, data was used from a radiosonde launched on the island of Kauai, HI, approximately 100 km away. Ten sequential spots at each angle were averaged to reduce the effect of noise, and then validation is done by subtracting this averaged brightness temperature from the simulated brightness temperature calculated with the radiosonde/dropsonde profiles.

Due to errors in position, time, assumed ancillary simulation inputs (e.g., surface temperature), and other sources, a single profile comparison can be misleading. Ideally, as many profile

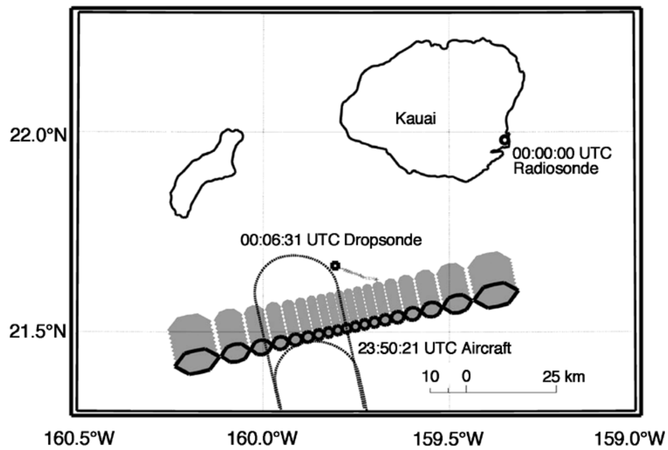

Fig. 4. Map with an example of the aircraft's position and the NAST-M's antenna footprints in relation to dropsonde and radiosonde release points. Also included are the UTC times of these releases, the aircraft's time of overpass, and the dropsonde's trajectory.

TABLE II
CALIBRATION RESULTS

Channel No.	183-GHz Spectrometer		425-GHz Spectrometer	
	mean difference (K)	standard deviation	mean difference (K)	standard deviation
1	-1.0	0.5	-0.60	0.5
2	-0.25	0.5	-0.55	0.5
3	0.05	0.6	-0.60	0.2
4	0.50	0.6	0.50	1.5
5	1.50	1.0	0.20	0.5
6	-0.05	1.0	1.50	1.5
7	N/A	N/A	-1.0	1.5

comparisons as possible are used and their statistics are calculated. The near-nadir mean and standard deviation statistics per channel are presented in Table II. The 425-GHz statistics utilized six radiosonde/dropsonde comparisons over two days during the PTOST 2003 mission. The 183-GHz system results utilized 13 dropsonde comparisons.

III. RAIN RATE AND CELL-TOP ALTITUDE ESTIMATION

In order to compare this novel NAST-M imagery to concurrent visible images, the NAST-M spectral images were converted to images of retrieved precipitation rain rate and cell-top altitude using the simple algorithm described below. The algorithm is only intended to give an overall understanding of the capabilities of the NAST-M spectrometers to retrieve precipitation parameters. More advanced algorithms for estimating these parameters from millimeter-wave spectral imagery have been previously described in [3], [9], and [10], but none have used the spectral range employed here.

The estimator is a weighted sum of first- and second-order polynomials of the difference between the observed brightness temperatures and the background (zero-cloud) temperatures, where the weights minimize the mean-square error over a training set. Third-order polynomials offered no discernible improvement. The noncloud background temperatures are easily determined from the NAST-M observations because of the modest size of the cells studied. All retrievals were trained and performed over ocean.

For each pixel, the retrieved parameter vector $\overline{P}$ (containing rain rate, precipitation cell-top altitude, and ice density) is simply related to the brightness perturbation vector $\overline{B} - \overline{M}$, where $(b_i - m_{b_i})$ is the ith vector element of $\overline{B} - \overline{M}$ corresponding to channel i, b_i is the observed brightness temperature, and m_{b_i} is the observed neighboring mean background (zero-cloud) brightness temperature

$$\hat{\overline{P}} = \overline{\overline{\mathbf{C}}} \cdot (\overline{B} - \overline{M}) + \overline{\overline{\mathbf{D}}} \cdot \overline{S}$$
$$\overline{S} = \left[(b_1 - m_{b_1})^2, (b_2 - m_{b_2})^2, \ldots, (b_N - m_{b_N})^2\right]^T. \quad (1)$$

$\overline{\overline{\mathbf{C}}}$ and $\overline{\overline{\mathbf{D}}}$ are $3 \times N$ matrices of weighting coefficients that minimize mean-square error over the chosen training dataset; N is the number of channels employed in the retrieval. The superscript T signifies the transpose operator.

The cloud model used to train this estimator used absorption coefficients from Liebe *et al.* [5] and a radiative transfer (RT) solution [11] that is not computation intensive for an altitude resolution of 500 m. The rain rates were linked to the drop-size distribution and total water density by the Marshall Palmer model [12]. The 15 cloud-top heights used for training ranged uniformly from 2–16 km, and the rain rates were 0.5, 1, 5, 10, 25, 50, 75, and 100 mm/h. Precipitation below freezing was assigned densities of 0.1, 0.4, 0.7, or 1 g/cm^3, which covered the range of snow, graupel, and ice; this density was also estimated using (1), but is not discussed further here. There was no correlation between assumed cloud-top altitude, rain rates, or ice densities, and it is assumed that physically plausible correlations would have improved the retrieval results. The temperature profiles were assumed to be the same inside and outside the clouds, whereas the relative humidity in the clouds was assumed to be 100%. These profiles were found by averaging a subset of the TIGR3 radiosonde set [13]. The subset was chosen to match the latitudes and months of the PTOST-2003 deployment. This distribution of precipitation parameters reasonably spans the range likely to be encountered in the field; for more realistic convective-cell profiles, see [14].

Because these retrievals are used in this paper primarily to illustrate the utility of the NAST-M observations and their relation to concurrent visible-wavelength data, more sophisticated retrieval methods were not warranted, particularly since the overflown precipitating-cloud ice-particle densities, habits, and size spectra were not measured simultaneously. The performance of this estimator for cell-top altitude and rain rate is suggested in Fig. 5, which compares model truth with the retrieval results obtained using (1) and the training dataset. The black dashed–dotted lines correspond to perfect retrievals, while the black line corresponds to a system using all of the NAST-M channels, the solid gray line characterizes a 183/425-GHz system, and the dashed gray represents the presently operational satellite system using 54 and 183 GHz. To allow the different spectrometers to be compared equally (i.e., limit the influence of the different receiver noise), each channel was given a radiometric sensitivity of 0.3 K (RMS). The error bars represent one standard deviation above and below the error's mean value, and the error bars were removed for rain rates under 25 mm/h in order to keep the figure

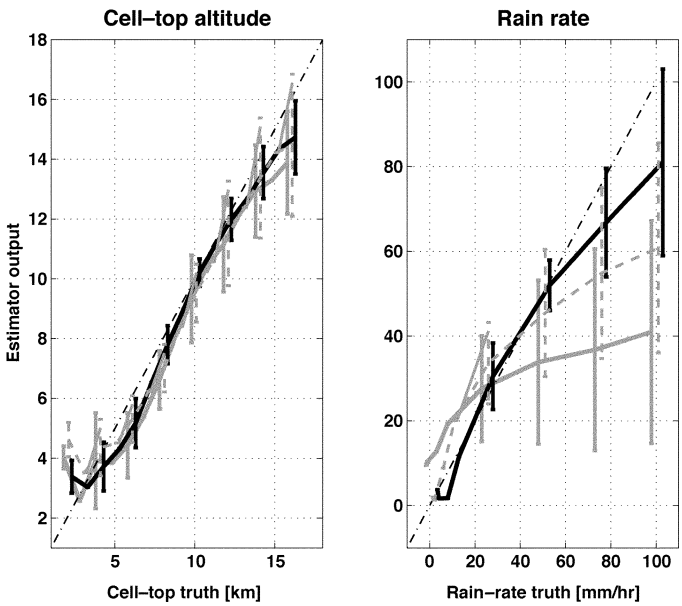

Fig. 5. Nonlinear estimator comparison between (black) a full complement NAST-M instrument, (gray) an estimator limited to the 183- and 425-GHz channels, and (dashed gray) a third case limited to 54- and 183-GHz channels.

clear. The averaged standard deviations for the first four rain rates (0.5–10 mm/h) were 7.0 mm/h for the full-band system, 9.4 mm/h for the 183/425-GHz system, and 8.3 mm/h for the 54/183-GHz system.

The curves in Fig. 5 suggest two points. First, all three systems are adequate to sound the precipitation cell-top altitude. Second, when estimating rain rate, the major contributions to the all-band equal-radiometric-sensitivity (27-channel) results came from the 54- and 118-GHz values for $\overline{\overline{\mathbf{C}}}$ and $\overline{\overline{\mathbf{D}}}$ in (1), plus the values for $\overline{\overline{\mathbf{C}}}$ for 183 GHz. The estimation of precipitation cell-top altitude used almost exclusively the values in $\overline{\overline{\mathbf{C}}}$. One important incidental lesson learned from this figure and by investigating the coefficient matrices is that single-pixel precipitation rate retrievals based exclusively on frequencies above 180 GHz may be impaired unless more sophisticated retrieval algorithms, more complex precipitation models, and superior radiative transfer solutions are used that correctly incorporate the correlations between rain rate, cell-top altitude, and convective cell diameter.

IV. Observations

A principal advantage of the NAST-M suite of microwave spectrometers is their superior response to the several degrees of freedom characterizing precipitation; each band contributes additional information useful in interpreting the responses of the others. The images presented here illustrate that capability.

The image in Fig. 6 was obtained while on Proteus near Miami, FL, during the CRYSTAL-FACE mission on July 13, 2002. The easternmost convective cell was imaged while the aircraft was banking, and therefore, the scattering is less prominent across all channels as the thickness of the atmosphere increased. The western cell illustrates the sensitivity of wavelength to hydrometeor diameter. This strong convective core is identified by the scattered signature in the 54-GHz channel,

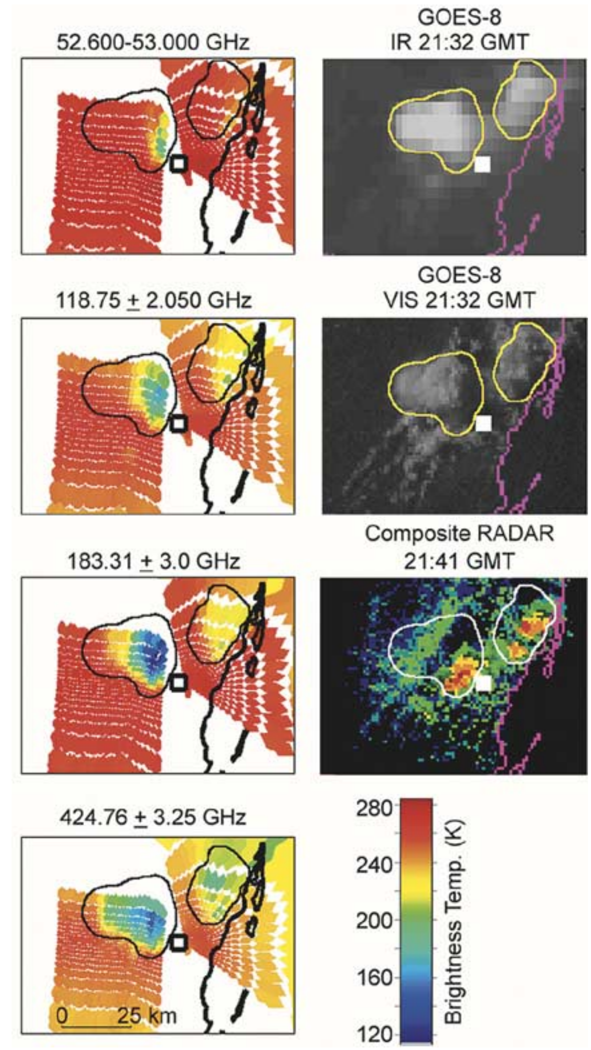

Fig. 6. Convective cell signature from microwave to visible wavelengths along with composite radar reflectivity on July 13, 2002 during CRYSTAL-FACE. Proteus crossed the main convective cell at 21:38 UTC. GOES and radar data courtesy of the Space Science and Engineering Center, University of Wisconsin–Madison.

because of the abundance of large diameter hydrometeors. As frequency increases, the cell signature enlarges to the extent of the infrared image, which is the limit of the cloud. The boundaries of the infrared signature were placed on the other images for comparison. The east-to-west increase in signature size could be an indication of westward blowoff from the wind shear at the top of the convective cell. The precipitation model described in Section III does not presently model the blowoff from a convective cell and the retrievals are not presented here.

The 183-GHz channel had the largest brightness-temperature perturbation, whereas the 425-GHz channel could see a high-altitude layer of small-diameter hydrometeors that do not perturb the lower frequency channels. When the microwave image is compared to the composite radar image, the 54-GHz channel matches the highest reflectivity region. While the airborne microwave instrument suggests the anvil blowoff, the ground based composite radar does not register the same precipitation on the surface. These discrepancies could arise from either instrument's blind spots or temporal differences.

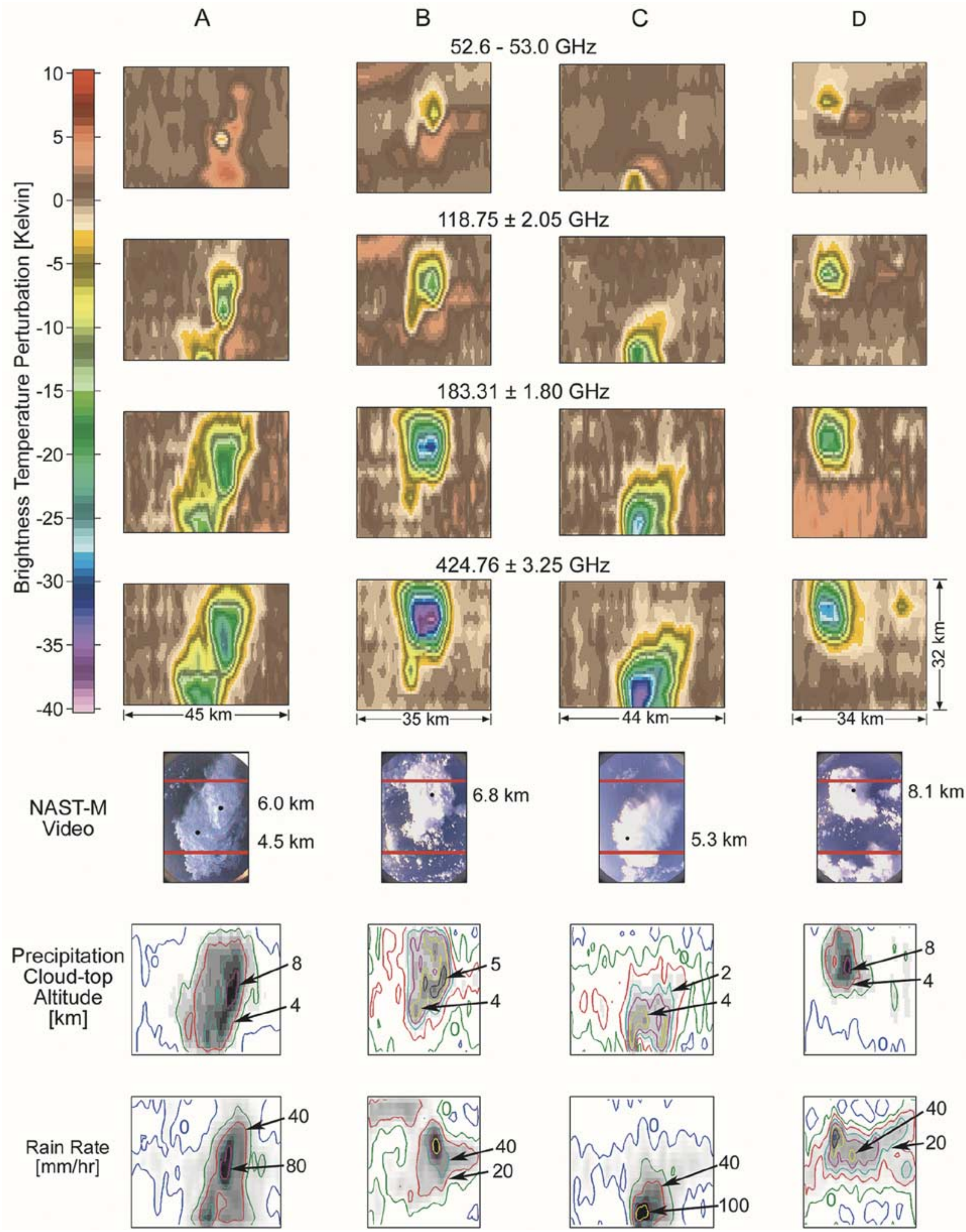

Fig. 7. Convective cell comparison with the NAST-M spectrometers between channels sharing similar clear-air temperature weighting functions. NAST-M video images of the clouds, precipitation cell-top altitude retrievals, and rain-rate retrievals are also presented. PTOST March 14, 2003.

Fig. 7 has further examples of convective cells, but they are less intense and smaller. For these cells, the retrieval technique from Section III was used to gain insight into the full-channel capability of NAST-M to retrieve precipitation parameters. The four columns of Fig. 7 correspond to four oceanic convective cells overflown on March 14, 2003 by the ER-2 at 20-km altitude over the North Pacific during PTOST 2003. The top four rows of the figure correspond to channels in the four bands that have weighting functions peaking at 1–4 km and have comparable cloud-free brightness temperatures. Only the innermost 11 angles are plotted; they span a swath approximately 32 km wide. The cloud-free baseline brightness temperature for each channel was subtracted to yield a cloud-perturbation image that simplifies interband comparisons.

The differences between the bands are striking. As in the previous image, the 52-GHz images clearly respond strongly only to the narrow convective cores of these cells where typical icy hydrometeors are sufficiently large to have strong scattering signatures, say more than two millimeters in diameter. The apparent width of these cores is approximately 9 km. The apparent diameters of the cells near 118 GHz are markedly larger because Rayleigh scattering (ice or liquid) is inversely proportional to the fourth power of wavelength. This trend continues as the frequency progresses to 183 and 425 GHz, for which these cell diameters approach approximately 16–17 km. A related trend continues for the minimum brightness temperatures at each of the cell tops. In order of increasing frequency, these minima are approximately 6, 18, 20–30, and 24–40 K below their baselines in all cases.

One potentially important implication of these results is that a diffraction-limited geostationary satellite with $\sim$20-km resolution at 425 GHz would sense pixels that are $\sim$5–10 K colder for each of the first three isolated cells, whereas the same antenna would yield pixels less than $\sim$2 K colder at 183-GHz or longer wavelengths. This difference would be the result of the increased spatial resolution, cell diameter, and Mie scattering near 425 GHz. Spatial resolution of 30 km or more can still be quite useful for the larger cell ensembles that typically dominate global rainfall, as is evident in the global rain images produced using the 54- and 183-GHz bands [10], [15].

The physical information content of such data is not readily evident from such perturbation images alone, however. The bottom two rows of Fig. 7 show the corresponding images of precipitation cell-top altitude and rain rate retrieved using (1) and the most transparent eight, six, six, and three channels in the four NAST-M spectrometers, in order of increasing frequency. Because the retrieval algorithm was derived for nadir viewing, only those 11 view angles within 36° of nadir are presented, corresponding to the area between the parallel lines shown in row five of the figure.

The retrieved cell-top altitudes are in reasonable agreement with those obtained by stereoscopy of the video images, as indicated by the dots and inferred altitudes shown in the fifth row of the figure. These retrieved cell-top altitude images topographically resemble the 425-GHz perturbation images more than the others, because the 0.7-mm wavelength is sensitive to the smallest hydrometeors. However, there is a significant difference between the precipitation cell-top altitude and rain-rate estimates. As expected, the highest rain-rate retrieved coincides with the 54-GHz channel's largest perturbation, while the perturbations at higher frequencies outline the lower-rain-rate regions. The model included only clear-air and convective cell profiles, and the estimator retrieved light precipitation in areas where the visible image showed low-lying clouds.

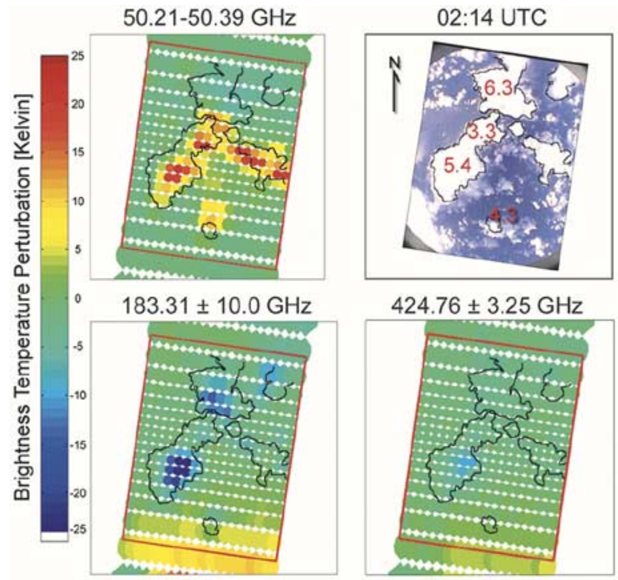

Fig. 8. NAST-M brightness temperature perturbations for the 54-, 183-, and 425-GHz window channels with a matching NAST-M video image. The clear-air brightness temperatures at nadir (limb) were 221 (242) K, 272 (266) K, and 251 (243) K for the 54-, 183-, and 425-GHz channels, respectively.

The 425-GHz brightness-temperature perturbation image corresponds well to the dynamically lifted portions of the visible cells, but exhibits little response to the surrounding lower clouds. An example of a failure to respond to lower clouds is illustrated in the upper left corner of column B where both the 52- and 118-GHz channels exhibit $\sim$2–5 K warming due to unglaciated precipitation or heavy clouds too low in the humid atmosphere to be sensed at either 183 or 425 GHz. The limited ability of 425-GHz channels to sense low-altitude clouds is further illustrated graphically in Fig. 8, which presents brightness temperature perturbations observed during a PTOST ferry flight over the North Pacific on March 14, 2003. The three window channels (i.e., the most transparent) of the 54-, 183-, and 425-GHz systems are shown together with a visible image. The perturbations are relative to clear air nearby, for which the brightness temperature at nadir and at the edge of the illustrated box are listed in the figure caption. The 425-GHz channel has a weighting function peaking near 4–5 km due to water vapor, which is at the top of these low-lying clouds. In dry atmospheres, 183-GHz channels penetrate to sea level, whereas the 425-GHz band almost never does.

V. Conclusion

The newly expanded NAST-M passive microwave spectrometer suite constitutes a valuable resource for imaging precipitation and atmospheric temperature and humidity profiles with spatial resolution and frequency coverage adequate to understand their radiative properties and to validate retrieval concepts.

Although soundings near 183 and 425 GHz are relatively less sensitive to the larger icy hydrometers (diameters greater than 2 mm) that signify strong convection and precipitation, they do respond strongly to the abundant smaller ice particles $\sim$1 mm in diameter that spread out from the convective cores of storms and remain visible longer at these shorter wavelengths. This longer lifespan aloft of smaller ice particles yields broader and stronger ice scattering signatures near 183 and 425 GHz from single isolated precipitation cells. This phenomenon makes any such unresolved cells much more evident near 183 and 425 GHz from diffraction-limited passive microwave sensors on satellites than they are at longer wavelengths.

These observations also demonstrate the importance of frequencies below ~173 GHz for sensing cloud water below ~3–4-km altitudes in the more tropical atmospheres; sensors near 425 GHz are of limited utility at those altitudes most everywhere, but significant convection penetrating above those levels is readily detected.

Finally, algorithms based on simple precipitation models yield plausible aircraft retrievals of cell-top altitude and rain rate consistent with available concurrent data. More sophisticated retrieval methods designed for these high frequencies could presumably perform better, particularly methods designed to capture the information content in the strong spatial differences between images obtained in different frequency bands.

ACKNOWLEDGMENT

The authors would like to thank P. Rosenkranz for his support of the instrument design and for assistance with radiance simulations; W. Blackwell for his thoughtful suggestions and insight; J. Barrett for his help and invaluable experience; J. Hesler, C. Eurvard (Millitech), and their associates for answering receiver questions; M. McGuirk and the MIT Central Machine Shop for the design and machine work; the employees at Scaled Composites and Dryden Flight Research Center for all their help, especially the crew and pilots of the Proteus and ER-2; J. Loparo and A. Sanchez for their work on NAST-M electronics; L. DiPalma for field support and RF work; and S. Bressler for his help with shipping and with the figures.

REFERENCES

[1] W. J. Blackwell, J. W. Barrett, F. W. Chen, R. V. Leslie, P. W. Rosenkranz, M. J. Schwartz, and D. H. Staelin, "NPOESS Aircraft Sounder Testbed-Microwave (NAST-M): Instrument description and initial flight results," *IEEE Trans. Geosci. Remote Sensing*, vol. 39, pp. 2444–2453, Nov. 2001.

[2] R. V. Leslie, "Temperature profile retrievals with the NAST-M Passive Microwave Spectrometer," Master's thesis, Dept. Electrical Eng. Comput. Sci., Massachusetts Inst. Technol., Cambridge, May 2000.

[3] M. S. Spina, M. J. Schwartz, D. H. Staelin, and A. J. Gasiewski, "Application of multilayer feedforward neural networks to precipitation cell-top altitude estimation," *IEEE Trans. Geosci. Remote Sensing*, vol. 36, pp. 154–162, Jan. 1998.

[4] W. J. Blackwell, "Retrieval of cloud-cleared atmospheric temperature profiles from hyperspectral infrared and microwave observations," Ph.D. dissertation, Dept. Electrical Eng. Comput. Sci., Massachusetts Inst. Technol., Cambridge, 2002.

[5] H. J. Liebe, P. W. Rosenkranz, and G. A. Hufford, "Atmospheric 60-GHz oxygen spectrum: new laboratory measurements and line parameters," *J. Quant. Spectrosc. Radiat. Transf.*, vol. 48, pp. 629–643, Nov. 1992.

[6] D. Cousins and W. L. Smith, "NPOESS airborne sounder testbed—interferometer," *Proc. SPIE*, vol. 3756, pp. 323–331, 1997.

[7] B. Bizzarri, A. Gasiewski, and D. H. Staelin, "Initiatives for millimeter/submillimeter-wave sounding from geostationary orbit," in *Proc. IGARSS*, vol. 1, 2002, pp. 548–552.

[8] J. L. Hesler, K. Hui, S. He, and T. W. Crowe, "A fixed-tuned 400 GHz subharmonic mixer using planar schottky diodes," in *Proc. 10th Int. Symp. Space Terahertz Technology*, Mar. 1999, pp. 95–99.

[9] G. Skofronick-Jackson and A. Gasiewski, "Nonlinear statistical retrievals of ice content and rain rate from passive microwave observations of a simulated convective storm," *IEEE Trans. Geosci. Remote Sensing*, vol. 33, pp. 957–970, July 1995.

[10] F. W. Chen and D. H. Staelin, "AIRS/AMSU/HSB precipitation estimates," *IEEE Trans. Geosci. Remote Sensing*, vol. 41, pp. 410–417, Feb. 2003.

[11] P. W. Rosenkranz, "Radiative transfer solution using initial values in a scattering and absorbing atmosphere with reflective surface," *IEEE Trans. Geosci. Remote Sensing*, vol. 40, pp. 1889–1892, Aug. 2002.

[12] J. S. Marshall and W. M. Palmer, "The distribution of raindrops with size," *J. Meteorol.*, vol. 5, pp. 165–166, 1948.

[13] J. Escobar, "Base de données pour la restitution de paramètres atmosphériques à l'échelle globale-etu de sur l'inversion per réseaux de neurones des données des sondeurs verticaux atmosphériques satellitaires présents et à venir," Ph.D. dissertation, Ecole Polytechnique, Toulouse, France, 1993.

[14] G. M. Skofronick-Jackson, A. J. Gasiewski, and J. R. Wang, "Influence of microphysical cloud parameterizations on microwave brightness temperatures," *IEEE Trans. Geosci. Remote Sensing*, vol. 40, pp. 187–196, Jan. 2002.

[15] F. W. Chen and D. H. Staelin, "Global precipitation climatology from AMSU passive microwave satellite observations," in *Proc. 14th Conf. Applied Climatology 84th Ann. Meeting Amer. Meteorological Soc.*, Seattle, WA, Jan. 2004, p. JP5.16.

R. Vincent Leslie (S'96) received the B.S. degree in electrical engineering from Boston University, Boston, MA, in 1998, and the S.M. degree in electrical engineering from the Massachusetts Institute of Technology (MIT), Cambridge, in 2000. He is currently pursuing the Sc.D. degree at MIT.

He is currently a Research Assistant for the Remote Sensing and Estimation Group, Research Laboratory of Electronics, MIT, and he has interned at the Raytheon Electronic Systems' Missile Radar Laboratory, Tewksbury, MA.

Mr. Leslie is a member of Tau Beta Pi and The Order of the Engineer.

David H. Staelin (S'59–M'65–SM'75–F'79) received the B.S., M.S., and Sc.D. degrees in electrical engineering from the Massachusetts Institute of Technology (MIT), Cambridge, in 1960, 1961, and 1965, respectively.

He joined the MIT Faculty in 1965, where he is a Professor of electrical engineering and teaches electromagnetics and signal processing. He was Principal Investigator for the NEMS and SCAMS microwave spectrometer experiments on the NASA Nimbus-5 and Nimbus-6 satellites and Co-Investigator for the NASA AIRS/AMSU/HSB sounding experiment on Aqua, the SMMR microwave experiment on Nimbus-7, and the Planetary Radio Astronomy Experiment on Voyager 1 and 2. He also served as Assistant Director of the MIT Lincoln Laboratory, Lexington, MA, from 1990 to 2001. Other research has involved radio astronomy, video coding, milliarc-second optical astrometry, and random-process characterization.